



1 **Aerosol radiative effects and feedbacks on boundary layer meteorology and**
2 **PM_{2.5} chemical components during winter haze events over the**
3 **Beijing-Tianjin-Hebei region**

4

5 Jiawei Li¹, Zhiwei Han^{*1,2}, Yunfei Wu¹, Zhe Xiong¹, Xiangao Xia³, Jie Li^{1,2}, Lin Liang^{1,2},
6 Renjian Zhang¹

7

8 ¹ Key Laboratory of Regional Climate-Environment for Temperate East Asia, Institute of
9 Atmospheric Physics, Chinese Academy of Sciences, Beijing 100029, China

10 ² University of Chinese Academy of Sciences, Beijing 100049, China

11 ³ Key Laboratory of Middle Atmosphere and Global Environment Observation, Institute of
12 Atmospheric Physics, Chinese Academy of Sciences,
13 Beijing 100029, China

14 Correspondence to: Zhiwei Han (hzw@mail.iap.ac.cn)

15

16 **Abstract**

17 An online-coupled regional chemistry/aerosol-climate model (RIEMS-Chem) was developed
18 and utilized to investigate the mechanisms of haze formation and evolution and aerosol
19 radiative feedback during winter haze episodes in February-March 2014 over the
20 Beijing-Tianjin-Hebei (BTH) region in China. Model comparison with a variety of
21 observations demonstrated a good ability of RIEMS-Chem in reproducing meteorological
22 variables, PBL heights, PM_{2.5} concentrations and its chemical components, as well as aerosol
23 optical parameters. It was noteworthy that the model performances were remarkably
24 improved for both meteorological variables and aerosol properties by taking aerosol radiative
25 feedback into account, highlighting the necessity of developing online coupled
26 chemistry-climate model. The weak southeasterly winds, high relative humidity and low PBL
27 height favored accumulation and secondary formation of aerosols, resulting in a maximum
28 daily and regional mean PM_{2.5} concentration exceeding 136 $\mu\text{g m}^{-3}$ in the BTH region. The
29 domain average aerosol radiative effects (AREs) were estimated to be -57 W m^{-2} at the
30 surface, 25 W m^{-2} in the atmosphere and -32 W m^{-2} at the top of atmosphere (TOA),



31 respectively, during the severe haze episode (20-26 February), and the maximum hourly ARE
32 at the surface reached -384 W m^{-2} in the vicinity of Shijiazhuang in southern Hebei province
33 during this episode. The average feedback-induced changes in 2-m air temperature (T2),
34 10-m wind speed (WS10), 2-m relative humidity (RH2) and planetary boundary layer (PBL)
35 height over the BTH region during the haze episode were $-1.8 \text{ }^\circ\text{C}$, -0.5 m s^{-1} , 10.0% and -184
36 m, respectively. The domain average changes in $\text{PM}_{2.5}$ concentration due to the feedback
37 were estimated to be $20.0 \text{ } \mu\text{g m}^{-3}$ (29%) and $45.1 \text{ } \mu\text{g m}^{-3}$ (39%) for the entire period and the
38 severe haze episode, respectively, and they were enhanced to $21.1 \text{ } \mu\text{g m}^{-3}$ (36%) and $49.3 \text{ } \mu\text{g}$
39 m^{-3} (49%) in terms of daytime mean during the haze episode, which demonstrated a
40 significant impact of aerosol radiative feedback on haze formation. The relative changes in
41 secondary aerosols were larger than those in primary aerosols, because chemical reactions
42 were also enhanced in addition to weakened diffusion by the feedback. The absolute change
43 in $\text{PM}_{2.5}$ concentrations caused by aerosol feedback was largest in the persistence stage,
44 followed by those in the growth stage and in the dissipating stage. Process analyses on haze
45 events in Beijing revealed that local emission, chemical reaction and regional transport
46 mainly contributed to haze formation in the growth stage, whereas vertical processes
47 (diffusion, advection and dry deposition) were major processes for $\text{PM}_{2.5}$ removals. Chemical
48 processes and local emissions dominated the increase in $\text{PM}_{2.5}$ concentrations during the
49 severe haze episode, whereas horizontal advection contributed to the $\text{PM}_{2.5}$ increase with a
50 similar magnitude to local emissions and chemical processes during a moderate haze episode
51 on 1-4 March. The contributions from physical and chemical processes to the
52 feedback-induced changes in $\text{PM}_{2.5}$ and its major components were explored and quantified
53 through process analyses. For the severe haze episode, the increase in the change rate of
54 $\text{PM}_{2.5}$ ($9.5 \text{ } \mu\text{g m}^{-3} \text{ h}^{-1}$) induced by the feedback in the growth stage was attributed to the larger
55 contribution from chemical processes ($7.3 \text{ } \mu\text{g m}^{-3} \text{ h}^{-1}$) than that from physical processes (2.2
56 $\text{ } \mu\text{g m}^{-3} \text{ h}^{-1}$), whereas, during the moderate haze episode, the increase in the $\text{PM}_{2.5}$ change rate
57 ($2.4 \text{ } \mu\text{g m}^{-3} \text{ h}^{-1}$) in the growth stage was contributed more significantly by physical processes
58 ($1.4 \text{ } \mu\text{g m}^{-3} \text{ h}^{-1}$) than by chemical processes ($1.0 \text{ } \mu\text{g m}^{-3} \text{ h}^{-1}$). In general, the aerosol-radiation
59 feedback increased the accumulation rate of aerosols in the growth stage through weakening
60 vertical diffusion, promoting chemical reactions, and/or enhancing horizontal advection. It



61 enhanced the removal rate through increasing vertical diffusion and vertical advection in the
62 dissipation stage, and had little effect on the change rate of PM_{2.5} in the persistence stage.

63

64 **1 Introduction**

65 Aerosols affect radiation transfer by scattering or absorbing solar and infrared radiation,
66 by acting as cloud condensation nuclei (CCN) to modify cloud properties, and by heating the
67 atmosphere to alter cloud formation, termed as the aerosol direct radiative effect, indirect
68 effect, and semi-direct effect (Twomey, 1974; Albrecht, 1989; Ramanathan et al., 2001),
69 respectively. In addition, there exists a set of interactions between chemistry, radiation and
70 meteorology (Dawson et al., 2007; Zhang, 2008; Isaksen et al., 2009; Baklanov et al., 2014;
71 Cai et al., 2017), which is highly complex and nonlinear and is currently one of the least
72 understood mechanisms in air pollution and climate change. The above interactions are not
73 included or not well treated in current atmospheric models.

74 Rapid and continuous growth of economy and energy consumption in the past decades
75 has greatly elevated aerosol levels in China (Chan and Yao, 2008; Zhang et al., 2012; Li et al.,
76 2017a), resulting in serious air pollution problem and potentially significant influence on
77 radiation and climate at multi-scales. Although emission control strategies have been
78 gradually implemented in recent years, haze events still often occur in east China, especially
79 in north China in wintertime due to both higher anthropogenic emissions and poorer
80 meteorological conditions. The haze pollution issue has attracted wide attentions from public,
81 government and scientific community in China and a lot of monitoring and modeling studies
82 have been carried out to explore the sources, characteristics, formation and evolution
83 mechanisms of haze events at both urban and regional scales (Chan and Yao, 2008; Zhang et
84 al., 2012; Che et al., 2014; Guo et al., 2014; Huang et al., 2014; Sun et al., 2014; Zheng et al.,
85 2015; Cheng et al., 2016; Ding et al., 2016; Li and Han, 2016a; Cai et al., 2017; Fu and Chen,
86 2017; Li et al., 2017b; Wang et al., 2017; Zhang et al., 2018a; Zhong et al., 2018a; Zhong et
87 al., 2018b; An et al., 2019; Li et al., 2019a), through which our understanding on haze
88 pollution has been promoted. However, there is still a large gap in our knowledge about haze
89 formation mechanism, in particular the role of aerosol-radiation-meteorology feedback in the



90 formation and evolution of haze pollution.

91 The aerosol radiative feedbacks on air quality and meteorology have ever been studied in
92 American and Europe with regional online coupled meteorology-chemistry models, such as
93 WRF-Chem (Grell et al., 2005; Zhang et al., 2010; Forkel et al., 2012), which demonstrates
94 an important role of the feedback in both air quality and meteorology. Carslaw et al. (2010)
95 also pointed out the complexity and significance of natural aerosol interactions and feedbacks
96 within the Earth system.

97 In east Asia, Han et al. (2013) revealed a significant feedback of mineral dust on dust
98 deflation and transport, atmospheric dynamics, cloud and precipitation in spring and an
99 improvement of model prediction for PM concentration and surface meteorology by the
100 inclusion of the feedback effect into an online coupled chemistry-aerosol-climate model. In
101 recent years, given the increasing concerns on haze pollution, some modeling studies have
102 been conducted to investigate the effect of aerosol radiative feedback on meteorology and
103 near surface PM_{2.5} concentration, with focus on winter haze events in north China (Wang et
104 al., 2014a; Wang et al., 2014b; Zhang et al., 2015; Gao et al., 2015; Gao et al., 2016; Qiu et
105 al., 2017; Zhao et al., 2017; Zhang et al., 2018b; Chen et al., 2019; Wu et al., 2019). Most of
106 the model results exhibited a positive feedback which tended to increase PM_{2.5} level, however,
107 the magnitude of such feedback differs largely, with the mean fractional change in PM_{2.5}
108 concentration varying from just a few percentage (Kajino et al., 2017; Wu et al., 2019) to
109 around 30% (Wang et al., 2014a). Some studies even show a negative feedback on PM_{2.5} in
110 Beijing (Zhang et al., 2015; Gao et al., 2016). Recently, Gao et al. (2020) reported that the
111 aerosol–radiation feedback-induced daytime changes in PM_{2.5} concentrations were less than 6%
112 during haze days in the BTH region in January 2010 from six applications of different online
113 coupled meteorology-chemistry models under the international framework of the MICS-Asia
114 (Model Inter Comparison Study for Asia) Phase III. There existed some differences in the
115 above modeling studies in terms of study period and haze pollution level, although they were
116 all for winter haze events in the BTH region. Zhong et al. (2018a) reported that over 70% of
117 PM_{2.5} increase during cumulative explosive stage of haze event in Beijing in winter can be
118 attributed to the feedback effect based on integrated analysis of observations. The above
119 studies highlight the importance and large uncertainties in the aerosol radiative feedback,



120 which require further model development and investigation.

121 The diversity in the feedback effect among models could be associated with the
122 differences in the predictions of aerosol chemical components and aerosol optical properties,
123 the assumption of mixing state and hygroscopic growth scheme, as well as meteorological
124 fields, all of which determine the direction and magnitude of the feedback effect. Previous
125 model studies consistently underpredict PM concentrations, especially for aerosol
126 components, such as sulfate, nitrate and SOA concentrations, mainly due to incomplete
127 understanding and unrealistic treatment of secondary aerosol formation through multi-phase
128 chemical processes. Gao et al., (2018) reported that most of the participating models
129 (including WRF-Chem) in the MICS-Asia (Model Inter Comparison Study for Asia) project
130 underpredicted inorganic and organic aerosol concentrations by up to a factor of three.
131 Besides aerosol mass concentration, the unrealistic representation of aerosol properties, such
132 as composition, size distribution, mixing state, hygroscopic growth would also lead to model
133 biases in aerosol optical properties and direct radiative effects. The low biases in the
134 predicted aerosol compositions may lead to underpredictions of aerosol optical depth (AOD)
135 and consequently of aerosol radiative effects and feedback. Che et al. (2014) reported a
136 reduction of solar radiation by aerosols exceeding 200 W m^{-2} during a severe haze event in
137 the north China Plain, much stronger than the estimations from models (around $\sim -100 \text{ W}$
138 m^{-2}). Therefore, a realistic treatment and an accurate representation of aerosol processes and
139 properties are crucial to the estimation of aerosol radiative effects and feedback.

140 It has been well recognized that high aerosol loadings can apparently reduce incoming
141 solar radiation at the surface, leading to surface cooling and inversion associated with
142 reduced wind speed and vertical diffusivity, and consequently increase in surface aerosol
143 concentrations. However, while we have gained considerable knowledge on the overall
144 feedback effect of aerosols, the detailed processes involved in the feedback mechanism are
145 still poorly understood and barely quantified, for example, how does the aerosol radiative
146 effect modify meteorological variables? how do the radiative and meteorological changes
147 affect physical and chemical processes and in turn affect the magnitude and distribution of
148 aerosol components? How to quantify the relative contributions from various physical and
149 chemical processes to the feedback effect?



150 In this study, an online coupled regional climate-chemistry-aerosol model (RIEMS-Chem)
151 was developed and applied to explore the formation and evolution of haze pollution during
152 February-March 2014, in which a week-long haze episode with the daily maximum PM_{2.5}
153 concentration up to 400 µg m⁻³ (hourly mean up to 483 µg m⁻³) was observed. A wide variety
154 of field measurements of aerosol chemical components, optical properties, as well as
155 meteorological variables were conducted and applied to develop, constrain and validate the
156 model. The mechanisms of haze formation and evolution, aerosol radiative effects and
157 feedback on meteorology and chemistry were investigated and assessed. The overall aerosol
158 feedback on PM_{2.5} and its aerosol compositions and the individual contributions to the
159 feedback from physical and chemical processes (advection, diffusion, deposition, chemistry,
160 etc.) during haze events were interpreted and quantified by a process analysis approach
161 incorporated in the model. The results from this study is expected to provide new insights
162 into the mechanism of aerosol-radiation-meteorology feedback, which is currently the source
163 of one of the largest uncertainties in haze pollution formation and evolution.

164

165 **2 Model and Data**

166 2.1 Model description

167 An online-coupled regional atmospheric chemistry/aerosol-climate model RIEMS-Chem
168 was used in this study, which was developed based on the Regional Integrated Environmental
169 Model System (RIEMS). A series of modules and parameterizations were adopted to
170 represent major physical processes, including a modified Biosphere-Atmosphere Transfer
171 Scheme (BATS; Dickinson et al., 1993) to simulate land surface process, the Medium-Range
172 Forecasts scheme (MRF) to represent the planetary boundary layer process (Hong and Pan,
173 1996), the cumulus convective parameterization scheme from Grell (1993), and a modified
174 radiation package of the NCAR Community Climate Model, version CCM3 (Kiehl et al.,
175 1996) to represent radiation transfer process including aerosol effect. RIEMS had been
176 applied to investigate East Asian monsoon climate and the interactions among physical,
177 biological and chemical processes (Xiong et al., 2009; Zhao, 2013; Wang et al., 2015).
178 RIEMS had participated in the Regional Climate Model Intercomparison Project (RMIP) for



179 Asia and it was one of the best models in predicting air temperature and precipitation over
180 east Asia (Fu et al., 2005).

181 The online-coupled model RIEMS-Chem has been developed in recent years by
182 incorporating major atmospheric chemistry/aerosol processes into the host model. Pollutants
183 are driven by meteorological fields provided by RIEMS and feedback to the existing dynamic
184 and physical modules (Han, 2010; Han et al., 2012). Major atmospheric processes including
185 emission, advection, diffusion, multi-phase chemistries, dry deposition and wet scavenging of
186 pollutants are considered. The advection and diffusion for pollutants are treated with the same
187 scheme for substances (such as moisture). Gas phase chemistry is represented by an updated
188 Carbon-bond mechanism (CB-IV; Gery et al., 1989). Thermodynamic processes are
189 calculated by the ISORROPIA II model (Fountoukis and Nenes, 2007). Dry deposition
190 velocity of aerosol is calculated by a size-dependent scheme which is expressed as the inverse
191 of the sum of resistance plus a gravitational settling term, while below-cloud wet scavenging
192 of aerosol is parameterized as a function of precipitation rate and collision efficiency of
193 particle by hydrometeor (Han et al., 2004). Heterogeneous reactions between gases and
194 mineral dust and sea salt aerosols have also been incorporated into RIEMS-Chem (Li and
195 Han, 2010; Li et al., 2018a). SOA formation is parameterized by a two-product model (Odum
196 et al., 1997).

197 Current atmospheric chemistry models generally tend to underpredict sulfate
198 concentrations, especially in source regions during wintertime, such as north China, which
199 could be due to uncertainties in the treatment of chemical formation mechanism. Recent
200 model studies suggested that heterogeneous reactions could be an important pathway in
201 sulfate formation during winter haze episodes in north China (Li et al., 2017c; Li et al.,
202 2018b). Therefore, heterogeneous reactions concerning the conversion of SO₂ to sulfate on
203 pre-existed hydrated aerosols were incorporated in RIEMS-Chem. The method of Li et al.
204 (2018b) was adopted, in which the uptake coefficient (γ_{SO_2}) was a stepwise function
205 determined by the aerosol water content (awc) which was predicted by the ISORROPIA II
206 model. Accordingly, the upper bound of awc was set to 300 $\mu\text{g m}^{-3}$ ($\gamma_{\text{SO}_2}=1\times 10^{-4}$) while the
207 lower bound was 30 $\mu\text{g m}^{-3}$ ($\gamma_{\text{SO}_2}=1\times 10^{-6}$). γ_{SO_2} was linearly interpolated between the upper
208 and lower bounds in terms of awc.



209 RIEMS-Chem treats 9 aerosol types including sulfate, nitrate, ammonium, black carbon
210 (BC), primary organic aerosol (POA), secondary organic aerosol (SOA), anthropogenic
211 primary PMs (PM_{2.5} and PM₁₀), dust and sea salt. The size distribution of the different types
212 of aerosols is previously prescribed based on the OPAC database (Optical Properties of
213 Aerosols and Clouds) (Hess et al., 1998). In this study, measurements in Beijing are used to
214 represent aerosol size distribution more realistically and to constrain the model. During the
215 study period, a scanning mobility particle sizer (SMPS; TSI, Inc., Shoreview, MN, USA) was
216 used to measure aerosol size distribution (Ma et al., 2017) and the geometric mean radius of
217 inorganic, black carbon and organic carbon aerosols were estimated to be 0.1 μm , 0.05 μm
218 and 0.1 μm , with standard deviations of 1.65, 1.6, 1.65, respectively. The above aerosol size
219 information was incorporated into RIEMS-Chem. The deflation of mineral dust is represented
220 by the scheme of Han et al. (2004) with 5 size bins (0.1–1.0, 1.0–2.0, 2.0–4.0, 4.0–8.0, 8.0–
221 20.0 μm). Primary PMs from anthropogenic are also assigned to the 5 size bins.

222 Recent observational analyses of aerosol mixing state in Beijing (Ma et al., 2012; Wu et
223 al., 2016) indicated that more than 80% aerosols were internally mixed with BC during haze
224 days, whereas about 70% of aerosols were externally mixed with BC in clean days, so an
225 internal mixing assumption was adopted in this study because the focus is paid on haze
226 episode.

227 A κ -Köhler theory (Petters and Kreidenweis, 2007) was used to parameterize aerosol
228 hygroscopic growth. In the model, the κ values for inorganic aerosols, BC, POA, SOA,
229 dust/primary PMs and sea salt were set to 0.65, 0, 0.1, 0.2, 0.01 and 0.98, respectively,
230 according to previous observational and modeling studies (Riemer et al., 2010; Liu et al.,
231 2010a; Westervelt et al., 2012).

232 The refractive index of an internally mixed aerosol is calculated by volume-weighting
233 the refractive indices of each aerosol component and water. Aerosol optical parameters
234 including extinction coefficient, single scattering albedo and asymmetry factor were
235 calculated by a Mie-theory based method developed by Ghan and Zaveri (2007), in which
236 aerosol optical parameters were pre-calculated with the Mie code and then fitted by
237 Chebyshev polynomials to create a lookup table of polynomial coefficients. By this way, the
238 calculation of aerosol optical parameters was much faster than using the traditional Mie



239 theory solution with a similar level of accuracy. This method has been successfully used in
240 the estimation of AOD over East Asia (Han et al., 2011a).

241 RIEMS-Chem has been successfully applied in previous modeling studies of
242 anthropogenic aerosols, mineral dust and marine aerosols regarding spatial-temporal
243 distributions, physical and chemical evolutions, radiative and climatic effects over east Asia
244 (Han et al., 2011b; 2012; 2013; 2019; Li et al., 2014; Li and Han, 2016b; 2016c; Li et al.,
245 2019b). RIEMS-Chem have been participating in the international model comparison project
246 Model Inter Comparison Study for Asia phase III (MICS-Asia III) and shows a good ability
247 in predicting PM_{2.5} concentration and AOD over East Asia (Gao et al., 2018).

248

249 2.2 Process analysis

250 In RIEMS-Chem, a time-splitting scheme based on continuity equation is applied to
251 predict species concentrations; therefore, the species concentrations are the net results of
252 successive changes in concentration due to different atmospheric physical and chemical
253 processes, and the changes in species concentration by each process can be recorded,
254 allowing the quantification of individual contribution of each process to species variation. In
255 this study, a process analysis (PA) scheme, which calculates the Integrated Process Rates
256 (IPR) at each time step and each grid, was embedded in RIEMS-Chem to identify the
257 contributions of physical and chemical processes to aerosol evolution. At each time step, the
258 IPR for a certain process was calculated by subtracting the species concentrations at the
259 beginning of this process from the ones after the process. The IPR method has ever been
260 applied to study the formation and fate of particulate and gaseous pollutants in North America
261 and China (e.g. Yu et al., 2008; Zhang et al., 2009; Liu et al., 2010b). The processes involved
262 in aerosol evolution include emissions of primary species, advections (horizontal and
263 vertical), diffusions (horizontal and vertical), dry deposition, chemical processes (gas-phase
264 chemistry, thermodynamic equilibrium and heterogeneous reactions), cloud processes and
265 wet deposition. Here cloud process represents the effects of cloud attenuation of photolysis
266 rate, aqueous-phase chemistry and in-cloud mixing. In this study, PA is applied not only to
267 quantify the contributions of individual physical and chemical processes to haze evolution,
268 but also to help interpret the processes involved in aerosol radiative feedback. In addition,



269 different from the previous PA application, chemical processes are further classified into gas
270 phase, thermodynamic and heterogeneous reactions to provide more details on chemical
271 pathways of secondary aerosol formation. The mass balance of IPR has been examined,
272 assuring that the change in species concentration during one time step is equal to the sum of
273 IPRs by each of the processes.

274

275 2.3 Emission inventories

276 Monthly mean anthropogenic emissions of sulfur dioxide (SO₂), nitrogen (NO_x),
277 ammonia (NH₃), non-methane volatile organic compounds (NMVOC), carbon monoxide
278 (CO), black carbon (BC), primary organic carbon (POA), other anthropogenic primary PM_{2.5}
279 and primary PM₁₀ in China for the year 2014 were obtained from the MEIC inventory
280 (Multi-resolution Emission Inventory for China) which was developed by Tsinghua
281 University (<http://meicmodel.org>). Anthropogenic emissions outside China were taken from
282 the MIX inventory which was developed to support the Model Inter-Comparison Study for
283 Asia phase III (MICS-Asia III) and the Hemispheric Transport of Air Pollution (HTAP)
284 projects (Li et al., 2017a). Both inventories of MEIC and MIX have the horizontal resolution
285 of 0.25 degree. Biomass burning emissions of aerosols and gas precursors for the year 2014
286 with a horizontal resolution of 0.25 degree were derived from the fourth version of the Global
287 Fire Emissions Database (GFED4) (Giglio et al., 2013). Monthly mean biogenic emissions of
288 isoprene and monoterpene were derived from Global Emissions Inventory Activity (GEIA,
289 <http://www.geiacenter.org/>). The above emission data were bilinearly interpolated to the
290 lambert projection of RIEMS-Chem.

291

292 2.4 Model configuration and numerical experiments

293 RIEMS-Chem was configured on a lambert conformal projection with horizontal
294 resolution of 60 km, covering most areas of China, the Korean Peninsula, Japan and part of
295 the Indo-China Peninsula (Figure 1). 16 vertical layers distributed vertically and unevenly in
296 the terrain-following sigma coordinate, with the lowest 8 layers within the boundary layer.
297 This study focused on the Beijing-Tianjin-Hebei (BTH) region with more attentions to the
298 Beijing metropolitan. The study period was from 10 February to 12 March, 2014,



299 encountering several haze episodes. The first 7 days were taken as model spin-up and the
300 results from 17 February to 12 March were used for analysis.

301 Initial and boundary conditions for meteorological variables were provided by the final
302 reanalysis data (FNL) with $1^\circ \times 1^\circ$ resolution and 6-hourly interval from the National Centers
303 for Environmental Prediction (NOAA/NCEP, 2000). Lateral boundary conditions of chemical
304 species at 6-hourly interval were derived from the simulations of the global chemical model
305 MOZART-4 (Model for Ozone and Related chemical Tracers, version 4; Emmons et al.,
306 2010).

307 To investigate the aerosol radiative effects and its potential feedback on solar radiation,
308 meteorological variables, planetary boundary layer (PBL) and aerosol concentrations in the
309 study domain, two simulations were designed. The FULL simulation (with aerosols)
310 considered all aerosol direct and indirect effects and feedbacks; the NoAer simulation
311 (without aerosols) shut off all aerosol radiative effects. In both simulations, the driving
312 meteorological data, emissions and model settings were exactly the same.

313

314 2.5 Observational data

315 Several observational datasets for meteorological variables, aerosol concentrations and
316 aerosol optical parameters were obtained and used for model comparison and analysis.

317 In-situ 3-hourly observations of temperature at 2 meter (T2), wind speed at 10 meter
318 (WS10) and relative humidity at 2 meter (RH2) from three meteorological monitoring sites
319 around Beijing (Figure 1) were collected from the China Meteorological Data Service Center
320 (CMDS) (<http://data.cma.cn/>).

321 To evaluate the model ability in reproducing evolution of planetary boundary layer
322 (PBL), high-frequency sounding data measured around 14:00 LST at the Xianghe station
323 ($39^\circ 45' \text{N}$, $116^\circ 58' \text{E}$; approximately 63 km southeast of Beijing downtown) were collected,
324 from which the PBL height can be determined based on the vertical gradients of virtual
325 potential temperature and water mixing ratio according to the method from Heo et al. (2003).
326 This sounding dataset provided a good indicator of mixing layer height because the sounding
327 was launched at 14:00 LST and lasts for about one hour. The meteorological sounding was
328 launched in Xianghe once a week (every Tuesday) and totally four soundings were available



329 during the study period (18 and 25 February, 4 and 11 March). Fortunately, the four
330 soundings encountered one severe haze episode, one moderate haze episode, and two clean
331 days, providing robust evidences on day-to-day variation of mixing layer height under
332 various atmospheric conditions. Hourly downward shortwave radiation flux (SWDOWN) at
333 the surface was measured simultaneously at the Xianghe station by a pyranometer with sun
334 shield and was used in this study.

335 The measurements of mass concentrations of PM_{2.5} and its components and aerosol
336 optical parameters were carried out at the tower division of the Institute of Atmospheric
337 Physics (IAP), Chinese Academy of Sciences (CAS) in Beijing (39°58'N, 116°22'E) from 17
338 February to 12 March, 2014. Real-time hourly PM_{2.5} mass concentrations were online
339 measured by a hybrid beta attenuation particulate monitor (Model 5030 SHARP, Thermo
340 Scientific, USA). PM_{2.5} samples were collected in parallel by an R&P Partisol® Model 2025
341 dichotomous sequential PM air sampler (Thermo, USA) and a MiniVol TAS PM sampler
342 (Airmetrics, USA) between 24 February and 12 March, 2014. Samples were collected twice
343 per day with one during the daytime (from 7:00 to 19:00 LST) and the other at night (from
344 19:00 to 7:00 of the next day). Totally 33 half-day samples were collected. Aerosol chemical
345 compositions including sulfate (SO₄²⁻), nitrate (NO₃⁻), ammonium (NH₄⁺), BC and OC were
346 analyzed by ion chromatography (Dionex ICS-90 for cations and ICS-1500 for anions) and a
347 DRI-2100A carbonaceous aerosol analyzer. Real-time hourly aerosol extinction coefficient
348 and aerosol absorption coefficient at dry condition (RH=10%) were synchronously measured
349 by a nephelometer (Aurora3000) and an aethalometer (AE-31), respectively. Detailed
350 information about this experiment including the sampling site, instruments, measurement
351 procedures and sample analysis were well documented in Ma et al. (2017). The mass
352 concentration of SOC was estimated using a revised EC tracer method (Zhao et al., 2013).

353 Measurements of AOD at the 4 sites (Nanjiao, Tianjin, Gucheng and Shangdianzi) in the
354 BTH region were obtained from the China Aerosol Remote Sensing Network (CARSNET)
355 (Che et al., 2014). Nanjiao is an urban site located in southern Beijing. Tianjin site is located
356 in the center of Tianjin city, about 120 km to the southeast of Beijing. Gucheng, a suburban
357 site in Hebei province, is about 130 km to the southwest of Beijing downtown. Shangdianzi is
358 located 150 km to the northeast of Beijing, which is a background station since it is far away



359 from anthropogenic sources. Daily mean AOD was derived by temporally averaging the raw
360 data measured by sunphotometer during daytime. To compare with the model output, AOD at
361 550 nm was used.

362

363 **3 Model validations**

364 3.1 Meteorological variables

365 Wind speed, temperature and relative humidity are key meteorological factors affecting
366 physical and chemical processes of atmospheric pollutants. The statistics for comparison
367 between in-situ observation and the FULL simulation for WS10, T2 and RH2 are presented in
368 Table 1. At the 3 sites (Beijing, Tianjin and Tanggu), the model performances were
369 reasonably good, although wind speeds were somewhat overpredicted. The overall
370 correlation coefficient (R) and normalized mean bias (NMB) at the 3 sites were 0.83 and -2%
371 for T2, 0.61 and -1% for RH2 and 0.47 and 31% for WS10. In all, RIEMS-Chem was able to
372 reasonably reproduce the meteorological variables during the study period. The statistics for
373 NoAer simulation are also list in Table 1. It is noteworthy that the statistics for the FULL
374 simulation are overall better than those for NoAer simulation, such as the warm bias in the
375 simulated air temperature and positive bias in wind speed are apparently reduced. This
376 demonstrates the inclusion of aerosol radiative effects does improve meteorological
377 prediction in this study.

378 The observed hourly SWDOWN in Xianghe was compared with model simulation
379 (Figure 2a). In general, the FULL case well reproduced SWDOWN in clean days and
380 light-moderate polluted days, but tended to underpredict observations in heavy haze days,
381 such as the period from 20 to 26 February. Underpredictions of cloud amount and PM
382 concentrations could be reasons for the low bias. For the entire study period, the observed
383 and simulated (FULL) mean SWDOWN were 136.0 W/m² and 188.4 W/m², respectively,
384 with R of 0.91 (Figure 2a). If only days with low cloud covers were considered, the
385 SWDOWNs were 183.3 W/m² and 213.7 W/m² from observation and the FULL case,
386 respectively, with the NMB of 16%. In contrast, the NoAer case failed to capture the
387 decreasing tendency of SWDOWN during haze days, resulting in a larger bias (NMB of 72%)



388 than the FULL case.

389

390 3.2 Planetary boundary layer (PBL) height

391 Figure 2b shows the simulated PBL heights at 14:00 LST from the FULL case and
392 NoAer case during the study period and the observed PBL heights at 14:00 LST determined
393 from air soundings on 18 February (clean), 25 February (severe haze), 4 March (clean) and
394 11 March (haze), 2014, respectively. There was large variation in PBL height in the afternoon,
395 with higher PBL height in clean days and lower one in haze days, inversely related to the
396 $PM_{2.5}$ level. The FULL case well reproduced the very low PBL height during the most severe
397 haze episode on 25 February, with the observed and simulated PBL heights to be 569m and
398 587m, respectively. In clean days, the much higher mixing layer was also well captured, such
399 as, on 4 March, the observed and simulated PBL heights were 2305m and 2535m,
400 respectively. It is noteworthy that the simulated PBL heights in the NoAer case were
401 consistently higher than those in the FULL case, and the PBL height simulation from the
402 FULL case (considering aerosol radiative effects) was apparently in a better agreement with
403 observation than that from the NoAer case, except for that on 18 February.

404

405 3.3 Mass concentrations of $PM_{2.5}$ and aerosol components

406 Figure 2c shows the hourly $PM_{2.5}$ mass concentrations observed at the IAP site and those
407 from the FULL simulation and NoAer simulation. The study period was characterized by
408 three haze episodes, which was the episode 1 on 20-26 February, the episode 2 from 1 to 4
409 March, and the episode 3 from 8 to 11 March. The first episode experienced the most severe
410 pollution with the maximum hourly $PM_{2.5}$ concentration exceeding $480 \mu\text{g m}^{-3}$ on 25
411 February. The second and third ones were moderately polluted in terms of magnitude and
412 lasting time. In general, the model reproduced the hourly variation of $PM_{2.5}$ concentrations
413 reasonably well in the FULL case, although the peaks were somewhat underpredicted in
414 some days, which could be partly due to the overprediction of wind speed (Table 1) and
415 potential uncertainties in emission inventories. The low bias in $PM_{2.5}$ concentrations could
416 also contribute to the overprediction of SWDOWN during the first haze episode (20-26
417 February) discussed in section 3.1. The average $PM_{2.5}$ concentrations during the study period



418 were $142.0 \mu\text{g m}^{-3}$ and $131.4 \mu\text{g m}^{-3}$ from observation and the FULL simulation, respectively,
419 with R of 0.8 and NMB of -7% (Table 2), which demonstrates a good model performance for
420 $\text{PM}_{2.5}$ predictions for the winter haze periods. A remarkable feature shown in Figure 2 is the
421 significant negative correlation between $\text{PM}_{2.5}$ concentration and PBL height and SWDOWN.

422 The comparison between the simulated daily mean surface aerosol components (sulfate
423 (SO_4^{2-}), nitrate (NO_3^-), ammonium (NH_4^+), BC and OC) and observations at the IAP site are
424 presented in Figure 3. The daily mean observation in the figure is an average of the half-day
425 samples, while the original half-day samples are used for statistics calculation in Table 2. The
426 model (from the FULL case) generally exhibits a good performance for inorganic aerosol
427 (sulfate, nitrate and ammonium) concentrations in terms of both daily variation and
428 magnitude (Figure 3a - 3c). It is encouraging that the maximum values on 25 February during
429 the first haze episode and the moderate values on 3 March in the second haze episode are
430 well reproduced, although some low biases occurred in the last few days. On average, the
431 model simulations of $20.3 \mu\text{g m}^{-3}$, $24.3 \mu\text{g m}^{-3}$ and $13.9 \mu\text{g m}^{-3}$ are very close to the
432 observations of $21.0 \mu\text{g m}^{-3}$, $26.0 \mu\text{g m}^{-3}$ and $14.1 \mu\text{g m}^{-3}$ for sulfate, nitrate and ammonium,
433 respectively, with Rs of 0.92, 0.88 and 0.91 and NMBs of -4%, -6% and -2%, respectively
434 (Table 2). Most of the online coupled models tended to underpredicted sulfate concentration
435 (Gao et al., 2016; Qiu et al., 2017; Gao et al., 2018), which led to an underestimation of
436 aerosol optical depth and radiative effect. The model in this study improves the simulation of
437 inorganic aerosols, mainly through the inclusion of heterogeneous chemical reactions for
438 inorganic aerosols.

439 The model also reproduced the temporal variation and magnitude of BC (Figure 3d) and
440 OC (Figure 3e) concentrations in Beijing reasonably well. However, the model tended to
441 underpredict the peak OC values on 24-25 February and to overpredict BC concentrations
442 from late February to early March. The low bias in OC simulation during the haze episodes
443 could be attributed to the underprediction of SOC (Figure 3f) due to potentially missing
444 chemical pathways. Uncertainties in the emission inventory could also be a reason. Li et al.,
445 (2017a) reported the uncertainties in BC and OC emissions for China could be $\pm 200\%$, larger
446 than those of emissions for gases ($< 70\%$) and primary PMs ($\sim 130\%$). The period mean BC
447 concentrations from observation and simulation were $5.2 \mu\text{g m}^{-3}$ and $6.7 \mu\text{g m}^{-3}$, respectively,



448 with R of 0.92 and NMB of 28% (Table 2). The period mean simulated and observed POC
449 concentrations were $18.4 \mu\text{g m}^{-3}$ and $15.5 \mu\text{g m}^{-3}$, respectively, with R of 0.93, whereas the
450 simulated SOC concentration was $9.9 \mu\text{g m}^{-3}$, lower than observation ($13.6 \mu\text{g m}^{-3}$) by 27%,
451 with a correlation coefficient of 0.56. For OC (sum of POC and SOC), the simulated value
452 ($28.3 \mu\text{g m}^{-3}$) was very close to the observation ($29.1 \mu\text{g m}^{-3}$), with R of 0.88 and NMB of
453 -3%, respectively, which indicated a generally good model performance for the total OC
454 concentration.

455 It is noteworthy that by considering aerosol radiative effects, the model apparently
456 improved simulations for both $\text{PM}_{2.5}$ and its chemical compositions, which is illustrated by
457 comparing model results between the FULL and NoAer cases (Figure 2c, Figure 3 and Table
458 2). Another important finding is that the duration of haze episode was prolonged by about 2-3
459 hours by the aerosol radiative feedback compared with that without aerosol feedback (Figure
460 2c).

461

462 3.4 Aerosol optical parameters

463 Figure 4a and 4b show the measured and simulated hourly aerosol extinction coefficient
464 (EXT) and aerosol absorption coefficient (ABS) at an RH of 10% at the IAP site during the
465 study period. It clearly showed that the model was able to well reproduce the magnitudes and
466 temporal variations of EXT and ABS under dry condition in the FULL case, although the
467 model tended to predict higher ABS in some days possibly due to the overprediction of BC
468 concentration. Single scattering albedo (SSA) which is defined as the ratio of scattering
469 coefficient (EXT minus ABS) to extinction coefficient is also given in Figure 4c. The FULL
470 case generally simulated high SSA values during haze episodes, such as 0.92 on 20-26
471 February, 0.85-0.9 from 1 to 4 March and 0.8-0.9 on 8-11 March, suggesting a dominant role
472 of light scattering aerosols in haze days. It is encouraging that the model reproduced SSA
473 during the severe haze episode (on 20-26 February) quite well, with both the simulation and
474 observation being approximately 0.92. However, SSA observation in clean days (such as on
475 5-7 March) was lower than that in haze days, and the model tended to overpredict SSA in
476 clean days, which could be attributed to uncertainties in measurement. In clean days, both the
477 denominator (EXT) and numerator (EXT minus ABS) were small, a subtle perturbation in



478 EXT and/or ABS can result in a large variation in SSA. A previous observational study in
479 Beijing suggested that SSA observation was more uncertain in clean days than in polluted
480 days because the observed aerosol extinction coefficient was too low in clean days (Jing et al.,
481 2015). On average, the observed EXT, ABS and SSA values were 0.51 km^{-1} , 0.048 km^{-1} and
482 0.85 , respectively, whereas, the corresponding FULL simulations were 0.53 km^{-1} , 0.052 km^{-1}
483 and 0.88 , with Rs of 0.8, 0.7 and 0.7 and NMBs of 4%, 10% and 5%, respectively (Table 2).
484 The above comparison demonstrates a good ability of the model in estimating aerosol optical
485 properties during the study period, which could be attributed to both the good performance
486 for aerosol compositions and the realistic representation of aerosol properties (aerosol size
487 distribution, mixing state, hygroscopic growth etc.), which is based on real-time
488 measurements in Beijing.

489 Besides EXT and ABS measured under dry condition, measurements of AOD at the four
490 CARSNET sites around Beijing (Nanjiao, Tianjin, Gucheng and Shangdianzi) were also used
491 to evaluate the model ability in simulating aerosol optical parameters in real atmosphere
492 (Figure 5). At the Nanjiao site, which is about 50km southeast of Beijing downtown (Figure
493 5a), AOD measurement was unavailable in most days during the first haze episode (20 to 26
494 February), with only two data (around 4.8) available on 25 February. The simulated daily
495 AOD from the FULL case varied from 3.1 to 4.0 during 24 - 26 February, somewhat lower
496 than the observation. The model tended to simulate lower AOD during the third haze episode
497 (8 to 11 March), which can be partly attributed to the predicted lower aerosol concentrations.
498 The measured AODs in Gucheng (southwest to Beijing) and Tianjin were similar in terms of
499 variation and magnitude (Figures 5b and 5c), showing high values during pollution periods
500 with the maximum daily AOD exceeding 4.0 in Gucheng and 3.5 in Tianjin. The FULL case
501 reproduced the AOD variations and magnitudes reasonably well at the two sites although low
502 biases still occurred during 8 to 11 March in Gucheng. For the regional background site
503 Shangdianzi (Figure 5d), the magnitude and variation of AOD were similar to those in
504 Nanjiao, suggesting that the haze episodes were regionally distributed because the temporal
505 variations and magnitudes of AOD were generally consistent at the four sites.

506 Table 3 summaries the performance statistics for daily mean AOD. In general, the model
507 reproduced the temporal variation and magnitude of AOD around Beijing reasonably well



508 with the overall R of 0.81 (0.67 ~ 0.90) and NMB of -8.6% (-15.6% ~ 6.2%). The
509 underestimation is mainly contributed by the low biases during the third haze episode (8 to 11
510 March) when inorganic aerosol concentrations were underestimated (Figure 3a-3c). In
511 addition, the limitation in AOD samples during the severe haze episode in Nanjiao and
512 Shangdianzi could amplify the negative bias. At the Gucheng and Tianjin sites where more
513 samples were available, the mean measured AODs were 1.7 and 1.4, respectively, agreeing
514 well with the simulated values of 1.5 and 1.3 from the FULL case.

515 In summary, the above comparisons demonstrate that RIEMS-Chem was capable in
516 reproducing the spatial distribution and temporal variation of meteorological variables (air
517 temperature, wind speed, surface shortwave radiation, PBL height etc.), concentrations of
518 total PM_{2.5} mass and its chemical compositions and aerosol optical properties during the
519 winter haze periods around Beijing. It is also noteworthy that the inclusion of aerosol
520 radiative effects apparently improved the overall model performance for both meteorological
521 variables and aerosol physical and chemical properties, highlighting the necessity to develop
522 online coupled chemistry-meteorology model for both air quality and climate research. The
523 good agreement above increases confidence in the reliability of the following model results
524 on aerosol radiative effects and feedback.

525

526 **4 Model results**

527 4.1 Distributions of meteorological variables and near surface PM_{2.5} concentration

528 The period-mean distributions of near-surface wind speed (WS10), temperature (T2),
529 relative humidity (RH2), PBL height and PM_{2.5} concentration are shown in Figures 6a to 6e.
530 During the study period, westerly winds dominated the northwestern parts of the BTH region
531 while southeasterly prevailed over the southeastern parts, as a result, the near-surface wind
532 speeds were fairly weak over the convergence zone from southern Hebei province to Beijing
533 (Figure 6c). Such wind pattern indicated that pollutants from southern parts of the domain
534 (such as Shandong and Henan provinces) can be transported northward to Beijing, Tianjin
535 and Hebei, and air pollutants over the weak-wind regions were easily accumulated to high
536 level. Near-surface temperature showed an apparent south-to-north gradient, with surface air



537 temperature in a range of 4 °C to 6 °C over the southern BTH region, -2 °C to 2 °C in the
538 vicinity of Beijing and parts of central Hebei, and lower than -2 °C in northern parts of the
539 domain (Figure 6a). Relative humidity was higher (~65% to 75%) over northern areas and
540 lower (~55% to 65%) over southern areas (Figure 6b). PBL height also exhibited an apparent
541 gradient in spatial distribution (Figure 6d), ranging from 800-1000 m in northern Hebei and
542 Inner Mongolia to about 600-700 m in southern Beijing, Tianjin and southern Hebei. A belt of
543 high PM_{2.5} concentration spread from southwest to northeast (Figure 6e), with the maximum
544 value up to 150 µg m⁻³ in the vicinity of Shijiazhuang and Beijing and Tianjin. The regions
545 with high PM_{2.5} concentrations generally corresponded well to the weak-wind areas shown in
546 Figure 6c.

547 Averaged over the BTH region and the entire study period, the simulated T2, WS10, RH2,
548 PBL height and PM_{2.5} concentration from the FULL case were 0.61 °C, 1.2 m s⁻¹, 67.0%,
549 698.4 m and 90.0 µg m⁻³, respectively. According to the “Technical Regulation on Ambient
550 Air Quality Index” prescribed by Chinese Ministry of Environmental Protection in 2012, a
551 pollution event occurs when 24-hr mean PM_{2.5} concentration ≥ 75 µg m⁻³. Totally, there were
552 11 days with domain and daily average PM_{2.5} concentration exceeding 75 µg m⁻³ in the BTH
553 region, with the maximum exceeding 136 µg m⁻³, indicating the severity of air pollution
554 during the study period.

555

556 4.2 Distributions of AOD, SSA and aerosol direct radiative effects

557 Figure 6f shows that high AODs mainly distributed from northern Beijing to
558 southwestern Hebei, southern Shanxi and northern Henan provinces, with the maximum up to
559 1.1. As AOD was determined by vertical profiles of aerosol compositions and RH, the spatial
560 distribution of AOD was somewhat different from that of PM_{2.5} concentration. During the
561 study period, the regional mean AOD in the BTH region was 0.78 (Table 4), about twice the
562 long-term observed value of about 0.4 in February and March in the same region (Song et al.,
563 2018).

564 The simulated SSAs were above 0.88 in the BTH region (Figure 6g), with relatively
565 lower values (0.88 - 0.9) in the areas of high PM_{2.5} concentration and higher ones (0.92 - 0.98)
566 in the relatively clean areas. On average, the simulated SSA in the BTH was 0.91 (Table 4),



567 within the range of 0.87 to 0.95 measured in the same region in January 2013 (Che et al.,
568 2014) but slightly lower than the model simulated annual mean of 0.95 over eastern China
569 (Zhuang et al., 2013).

570 All-sky aerosol radiative effects at the surface (ARE_{surf}), at the top of atmosphere
571 (ARE_{TOA}) and in the atmosphere (ARE_{atm}) under all-sky condition are presented in Figures 6h
572 to 6j. During the study period, aerosols induced a negative ARE both at the surface and TOA
573 and a positive ARE in the atmosphere over the BTH. The distribution of ARE resembles that
574 of AOD, generally showing stronger effects over southwestern Hebei, Shanxi and northern
575 Henan provinces where high AOD occurred. Moderate AREs appeared over Beijing, Tianjin
576 and central Hebei, while relatively weak AREs appeared over the northern domain. The
577 domain average AREs in the BTH region during the period were estimated to be -37 W m^{-2} ,
578 19 W m^{-2} and -18 W m^{-2} at the surface, in the atmosphere and at the TOA, respectively (Table
579 4). The indirect radiative effect was also estimated to be about -2 W m^{-2} at the surface and the
580 TOA on average, much smaller than the direct radiative effect; therefore, the total radiative
581 feedback is predominated by direct radiative effect during the study period.

582 The domain average all-sky AREs during the first haze episode (20-26 February) were
583 -57 W m^{-2} , 25 W m^{-2} and -32 W m^{-2} at the surface, in the atmosphere and at the TOA,
584 respectively, and the values were further enhanced to -123 W m^{-2} , 53 W m^{-2} and -70 W m^{-2} in
585 terms of daytime mean. The maximum AREs at the surface and at TOA reached -384 W m^{-2}
586 and -231 W m^{-2} , respectively, at 13:00 LST on 23 February in the vicinity of Shijiazhuang.

587 In Beijing, the estimated mean AREs were -70 W m^{-2} , 32 W m^{-2} and -38 W m^{-2} at the
588 surface, in the atmosphere and at the TOA, respectively, during the first haze episode,
589 whereas the maximum ARE at the surface reached -304 W m^{-2} at 13:00 LST on 22 February,
590 which was associated with the high $PM_{2.5}$ concentration ($453 \mu\text{g m}^{-3}$) at that time.

591 Based on in-situ surface measurements, Che et al. (2014) estimated that during haze
592 periods in January 2013, the mean daytime AREs at Nanjiao and Xianghe were
593 approximately -42 W m^{-2} and -50 W m^{-2} at TOA, and -120 W m^{-2} at the surface at both sites.
594 In this study, the daytime AREs averaged over the severe haze period (20-26 February) at
595 TOA were estimated to be -77 W m^{-2} and -74 W m^{-2} at Nanjiao and Xianghe, while the
596 corresponding AREs at the surface were -146 W m^{-2} and -140 W m^{-2} , respectively. Che et al.



597 (2014) also reported the maximum daily mean surface ARE of -220 W m^{-2} at Nanjiao during
598 a severe haze episode in January 2013, in this study, the corresponding ARE was estimated to
599 be approximately -200 W m^{-2} at the same site during the severe haze episode in February
600 2014. Therefore, the magnitudes of AREs during haze episodes simulated from this study
601 agreed favorably with the above observational based estimations around Beijing, despite the
602 different time period.

603

604 4.3 Impacts of aerosol radiative feedback on meteorological variables and aerosols

605 Figure 7a-7e shows the mean differences in T2, RH2, wind speed, PBL height and near
606 surface $\text{PM}_{2.5}$ concentration induced by the radiative feedback due to all aerosols (FULL
607 minus NoAer) in the domain during the study period.

608 The aerosol radiative effects led to a reduction in surface shortwave radiation and thus
609 surface air temperature in the entire domain. The magnitude of T2 variation decreased from
610 south to north of the BTH, with $-1.6 \text{ }^{\circ}\text{C}$ to $-2 \text{ }^{\circ}\text{C}$ in southern Hebei and $-1.2 \text{ }^{\circ}\text{C}$ to $-1.8 \text{ }^{\circ}\text{C}$ in
611 southern Beijing, respectively. Correspondingly, RH2 increased by 10%-16% in the above
612 regions. The changes in wind speed showed a patchy pattern, with decreases by $\sim 0.1 \text{ m s}^{-1}$ in
613 southern Hebei, increases by $\sim 0.2 \text{ m s}^{-1}$ in central Hebei, and decreases in most parts of
614 Beijing. Wind vector shows an anomalous northerly wind of $\sim 0.5 \text{ m s}^{-1}$ in the BTH region.
615 Due to the reduction in surface shortwave radiation, PBL height decreased over the entire
616 region, with the maximums up to 240 m in southern Hebei and northern Tianjin. The changes
617 in PBL height varied from -210 m in southern Beijing to -90m in northern Beijing. $\text{PM}_{2.5}$
618 concentrations were consistently enhanced over the entire region, with the maximum increase
619 up to $33 \text{ } \mu\text{g m}^{-3}$ in southern Hebei and portions of Beijing and Tianjin. In most of the BTH
620 region, the percentage increase of $\text{PM}_{2.5}$ exceeded 25%, with the maximum increase
621 exceeding 33% in the vicinity of Shijiazhuang. It is of interest that the regions with the
622 maximum increase of $\text{PM}_{2.5}$ generally corresponded to those with the maximum decrease in
623 PBL height. The presence of aerosols reduced solar radiation reaching the ground surface,
624 resulting in decreases in surface air temperature and PBL height and an increase in relative
625 humidity, all of which favored accumulation and formation of aerosols due to weakened
626 vertical mixing and enhanced secondary aerosol formation.



627 The aerosol feedback during the first haze episode was further explored due to the much
628 higher $PM_{2.5}$ level than the period average. Figure 7f-7j show the mean changes in
629 meteorological variables and $PM_{2.5}$ concentrations during the first haze episode (20-26
630 February). In general, the changes induced by aerosol feedback were larger during the severe
631 haze episode than those over the entire study period. T2 decreased by 1.8 °C to 2.7 °C along
632 with an increase up to 20% in RH in southern Hebei and southern parts of Beijing and Tianjin.
633 Different from the entire period average, wind speed decreased consistently in the BTH, with
634 a maximum decrease of 1 m s⁻¹. PBL height decreased by ~300 m in southern Hebei,
635 corresponding to the areas with large air temperature decrease. This resulted in a consistent
636 increase in $PM_{2.5}$ concentrations in the study domain, with the maximum increases exceeding
637 50% around Shijiazhuang and approximately 40% in Beijing and Tianjin, apparently higher
638 than the entire period averages. If for daytime mean, the percentage changes of $PM_{2.5}$ in the
639 above areas increased to 70% and 60%, respectively (figure not shown). It is striking that the
640 simulated maximum increase in hourly $PM_{2.5}$ concentration can be up to 372 $\mu\text{g}/\text{m}^3$ (186%)
641 in the vicinity of Shijiazhuang at about 10:00 LST on 24 February during the first haze
642 episode, which demonstrates the substantial impact of the radiative feedback on $PM_{2.5}$
643 concentration and haze formation.

644 It is worthwhile to further explore the effect of aerosol feedback during haze evolution.
645 We divided haze episode into three stages, the growth stage is defined as the time period of
646 $PM_{2.5}$ increase from clean condition to heavy pollution level, the persistence stage means the
647 duration period of haze and the dissipation stage means the period with a sharp decrease in
648 $PM_{2.5}$ concentration usually along with a cold front passage. During the first heavy haze
649 episode (20-26 February) in Beijing, aerosol radiative feedback caused the increases in $PM_{2.5}$
650 concentration of 55 $\mu\text{g m}^{-3}$, 84 $\mu\text{g m}^{-3}$ and 40 $\mu\text{g m}^{-3}$, with the fractional changes of 31%, 41%
651 and 67%, respectively, during the growth, persistence and dissipation stages. The larger
652 fractional change of $PM_{2.5}$ in the dissipation stage is due to the relatively large
653 feedback-induced increase and the lowest $PM_{2.5}$ concentration in the NoAer case in this stage.
654 During the second haze episode (1-4 March), the increases in $PM_{2.5}$ concentration due to
655 aerosol feedback were 25 $\mu\text{g m}^{-3}$, 45 $\mu\text{g m}^{-3}$ and 24 $\mu\text{g m}^{-3}$, with the fractional changes of
656 21%, 35% and 34%, respectively, which are lower than the feedback effect during the first



657 haze episode. So, in terms of magnitude, the largest feedback effect on $PM_{2.5}$ occurred in the
658 persistence stage, followed by that in the growth stage, although the fractional change of
659 $PM_{2.5}$ was larger in the dissipation stage.

660 Table 5 summarized the average feedback-induced changes in meteorological variables
661 and $PM_{2.5}$ concentrations over the BTH region during the entire and the first haze periods.
662 During the study period, due to the radiative feedback by all aerosols (FULL minus NoAer),
663 surface air temperature and wind speed decreased by $1.4\text{ }^{\circ}\text{C}$ and 0.04 m s^{-1} , respectively, with
664 RH increased by 8.7% in the BTH. PBL height was reduced by 160 m (or a percentage
665 change of -18.6%) on average, along with a reduction of $3.3\text{ m}^2\text{ s}^{-1}$ (-27.0%) in vertical
666 diffusivity coefficient (K_z), resulting in an increase of $PM_{2.5}$ level by $20.0\text{ }\mu\text{g m}^{-3}$ (28.6%). It
667 is noticed that the above changes were strengthened during the severe haze episode on 20-26
668 February, with the 7-day average decreases in T2, WS10, PBL height and K_z being up to -1.8
669 $^{\circ}\text{C}$, -0.5 m s^{-1} , -183.6 m (-31.0%) and $3.9\text{ m}^2\text{ s}^{-1}$ (-48.8%), respectively, and the $PM_{2.5}$
670 concentration increased by $45.1\text{ }\mu\text{g m}^{-3}$ with a percentage increase of 38.7%. Because
671 aerosols affect solar radiation in daytime, in term of daytime mean, the 7-day mean changes
672 in T2, WS10 and PBL height were estimated to be $-2.5\text{ }^{\circ}\text{C}$, -0.6 m s^{-1} and -307.3 m (-37.6%),
673 respectively, leading to an increase of $49.3\text{ }\mu\text{g m}^{-3}$ (48.5%) in $PM_{2.5}$ concentration.

674 The impact of aerosol radiative feedback in Beijing (Table 6) was stronger than the
675 regional mean. During the first haze episode, the 7-day average changes in T2, WS10, RH2,
676 PBL and $PM_{2.5}$ were estimated to be $-2.1\text{ }^{\circ}\text{C}$, -0.6 m s^{-1} , 17.0%, -195.6 m (-35.9%) and 68.0
677 $\mu\text{g m}^{-3}$ (39.1%), respectively, and the daytime mean change in $PM_{2.5}$ concentration increased
678 to $83.2\text{ }\mu\text{g m}^{-3}$ (60%), respectively.

679 Table 7 presents the average changes in major aerosol components (BC, sulfate and
680 nitrate) in $PM_{2.5}$ induced by the feedback effect. Over the BTH region, the feedback caused
681 the average increases in sulfate and nitrate by $5.0\text{ }\mu\text{g m}^{-3}$ (46.4%) and $6.8\text{ }\mu\text{g m}^{-3}$ (37.3%),
682 respectively, for the entire period, and by up to $12.6\text{ }\mu\text{g m}^{-3}$ (66.9%) and $14.6\text{ }\mu\text{g m}^{-3}$ (40.9%),
683 for the first haze episode. The feedback-induced increases in BC was $0.9\text{ }\mu\text{g m}^{-3}$ (25.1%) and
684 $1.9\text{ }\mu\text{g m}^{-3}$ (32.9%), respectively, for the entire period and the first haze episode. It was
685 noticed that the feedback-induced changes in sulfate and nitrate concentrations were larger
686 than that in BC concentration. This was because that the concentrations of secondary aerosols



687 were increased not only by weakened vertical diffusivity but also by enhanced chemical
688 reactions due to the radiative feedback, which will be discussed in detail in section 5.2.

689 The above analysis demonstrates a significant impact of aerosol feedback on $PM_{2.5}$
690 concentration during winter haze episodes in the BTH region. Previous modeling studies
691 reported different degrees of aerosol radiative feedback in east China. Gao et al. (2015)
692 simulated an increase of near surface $PM_{2.5}$ concentrations to be 10-50 $\mu\text{g m}^{-3}$ or 5-25% in the
693 BTH during a severe haze episode on 10-15 January 2013 by using WRF-Chem. For the
694 similar time period and region, Wang et al. (2014a) reported an increase in $PM_{2.5}$
695 concentrations by 15-50 $\mu\text{g m}^{-3}$ or 10-30% by using a regional coupled model NAQPMS. Wu
696 et al. (2019) used WRF-Chem to investigate a haze episode from 5 December 2015 to 4
697 January 2016 in the North China Plain and found that the aerosol radiative effects can
698 enhance near-surface $PM_{2.5}$ concentration by 10.2 $\mu\text{g m}^{-3}$ (7.8%) on average.

699 The results from this study demonstrate a stronger aerosol-radiation feedback than
700 previous modeling studies, with an average increase in $PM_{2.5}$ concentration by up to 45.1 μg
701 m^{-3} (38.7%) during a severe haze episode and further to 49.3 $\mu\text{g m}^{-3}$ (48.5%) for daytime
702 mean over the BTH region. This study also highlights that the aerosol feedback effect can
703 result in an increase of hourly $PM_{2.5}$ concentrations by up to 372 $\mu\text{g m}^{-3}$ (186%) in the
704 vicinity of Shijiazhuang during the severe haze episode. The stronger feedback effect in this
705 study than previous model simulations is mainly due the predicted higher concentration of
706 aerosol components (especially inorganic aerosols) and aerosol optical properties, which are
707 also in a better agreement with observations. It is noticed that a recent study (Zhong et al.,
708 2018a) reported that the aerosol feedback effect contributed over 70% to $PM_{2.5}$ increase
709 during the cumulative explosive stage of haze event in winter Beijing based on integrated
710 analysis of observations from 2013-2016, which suggested a dominant role of the feedback
711 effect in haze formation.

712

713 **5 Process analysis of haze evolution and aerosol radiative feedback**

714 The process analysis (PA) method calculates the Integrated Process Rates (IPRs) and is
715 applied to quantify the individual contributions of different physical and chemical processes



716 to variations of PM_{2.5} and its chemical components. These processes include emission,
717 horizontal and vertical advections (HADV and VADV), horizontal and vertical diffusions
718 (HDIF and VDIF), dry deposition (DDEP), cloud (CLD, including aqueous chemistry and
719 wet scavenging), gas chemistry (GAS), thermodynamic chemistry (Thermo) and
720 heterogeneous chemistry (HET). The focus of this study is Beijing, so the model grid cell
721 near the surface having Beijing is selected for analysis.

722

723 5.1 The mechanism of haze evolution related to various processes

724 5.1.1 Haze evolution during 20-26 February

725 There was a severe haze event lasting for about 7 days, with the maximum hourly PM_{2.5}
726 up to 482 µg m⁻³ on 26 February. This haze was initially formed on 20 February, with the
727 observed surface PM_{2.5} concentration less than 50 µg m⁻³ on 19 February, rapidly increased to
728 343 µg m⁻³ on 20 February, and reached 482 µg m⁻³, followed by rapid haze dissipation on 26
729 February due to the arrival of a cold front.

730 PA was used to provide insights into the evolution mechanism of the haze episode, which
731 was divided into the clean, growth, persistence and dissipation stages in this study. Figure 8
732 shows the average process budgets for changes in PM_{2.5} (which is the sum of sulfate, nitrate,
733 ammonium, BC, OC, SOC and primary PM_{2.5}) and its major components in Beijing during
734 the four stages of the first haze period (Figure 8) from the FULL simulation. Figure 8a shows
735 the hourly IPRs of PM_{2.5} by physical and chemical processes. The emission of primary
736 aerosols was the largest contributor to the PM_{2.5} mass with a constant IPR of 29.8 µg m⁻³ h⁻¹
737 (not shown in Figure 8a for clarity) due to the use of a monthly based emission inventory.
738 Chemical processes (GAS, Thermo and HET) also contributed largely to PM_{2.5}, with
739 generally larger contributions in the growth and persistence stages. Thermodynamic
740 equilibrium processes and gas chemistry accounted for over 2/3 of the chemical contributions,
741 with the former process mainly accounting for the formation of nitrate and ammonium and
742 the latter one for sulfate formation. The contribution from heterogeneous reactions was
743 generally small, but when conditions were favorable (such as high RH and high aerosol
744 concentration providing sufficient reaction surfaces), its contribution would also be
745 significant, such as on the morning of 22 February, at nighttime from 23 to 24 February, and



746 on the mornings of 25 and 26 February. Vertical diffusion and dry deposition consistently
747 removed $PM_{2.5}$ from the atmosphere. In general, the larger IPRs from both VDIF and DDEP
748 during the clean and dissipation stages resulted in lower $PM_{2.5}$ concentrations, whereas the
749 lower IPRs from VDIF and DDEP in the growth stage favored aerosol accumulation. In the
750 persistence stage, the IPRs of VDIF and DDEP were generally small. It should be noted that
751 on every midday, when PBL was fully developed, the vertical diffusion reached the daily
752 maximum, producing distinctly large negative IPRs of VDIF. Advections (HADV and VADV)
753 and horizontal diffusion either contributed to the accumulation or loss of $PM_{2.5}$. During this
754 severe haze episode, horizontal diffusion served as a sink of $PM_{2.5}$, producing a negative IPR
755 of HDIF through the event. Horizontal advection served as a sink of $PM_{2.5}$ in most of the time,
756 leading to a negative IPR of HADV, however, when the removal of $PM_{2.5}$ by vertical
757 diffusion was strong at the midday, aerosols were advected to Beijing from surrounding areas
758 due to mass balance, resulting in a positive IPR of HADV. The positive IPR of VADV during
759 the growth and persistence stages of this event indicated that the downward transport of
760 aerosols from upper levels also contributed to the $PM_{2.5}$ increase, such as on the mornings of
761 22 and 25 February. In general, the IPRs (represented the net effect of all processes, denoted
762 by the red line in Figure 8a) exhibited small positive values from evening to next morning on
763 every day, indicating a gradually increasing $PM_{2.5}$ concentration, whereas on every midday,
764 relatively large negative IPRs occurred, indicating an apparent decrease in $PM_{2.5}$
765 concentration at that time. It should be mentioned that even in the persistence stage, the
766 diurnal variation of $PM_{2.5}$ occurred although the change rates were generally weaker than
767 those in the growth and dissipation stages.

768 Figure 8b to 8f show the mean IPRs for $PM_{2.5}$ and its major chemical components as well
769 as the key meteorological variables averaged over each stage to help interpret the formation
770 and evolution mechanism of this severe haze episode.

771 In the clean stage, emission and chemistry were the two major processes for $PM_{2.5}$
772 production (Figure 8b). Emission contributed predominately to $PM_{2.5}$ production (IPRs of
773 $29.8 \mu\text{g m}^{-3} \text{h}^{-1}$), whereas the contributions of gas ($9.2 \mu\text{g m}^{-3} \text{h}^{-1}$) and thermodynamic
774 chemistry ($7.3 \mu\text{g m}^{-3} \text{h}^{-1}$) were comparable. The most influential process for $PM_{2.5}$ removal
775 was vertical diffusion, with the IPRs of $-30.3 \mu\text{g m}^{-3} \text{h}^{-1}$, comparable to that of emission. Dry



776 deposition was the second most important process for $\text{PM}_{2.5}$ loss ($-12.2 \mu\text{g m}^{-3} \text{h}^{-1}$), followed
777 by horizontal diffusion. Advection had a negligible effect on $\text{PM}_{2.5}$ in this stage. In the growth
778 stage, it is noteworthy that the contributions from vertical diffusion (VDIF) and dry
779 deposition (DDEP) to $\text{PM}_{2.5}$ removal decreased markedly from $-30.3 \mu\text{g m}^{-3} \text{h}^{-1}$ and $-12.2 \mu\text{g}$
780 $\text{m}^{-3} \text{h}^{-1}$ in the clean stage to $-21.6 \mu\text{g m}^{-3} \text{h}^{-1}$ and $-9.2 \mu\text{g m}^{-3} \text{h}^{-1}$, respectively (Figure 8b),
781 mainly due to the decrease in wind speed and the increase in stability indicated by the
782 reduced vertical diffusivity coefficient K_z (Figure 8f), leading to increases in concentrations
783 of all species. It is impressive that the contributions from chemical processes
784 (GAS+Thermo+HET) increased apparently compared with those in the clean stage, with the
785 IPRs from gas, thermodynamic and heterogeneous chemistry increase to $12.1 \mu\text{g m}^{-3} \text{h}^{-1}$, 16.0
786 $\mu\text{g m}^{-3} \text{h}^{-1}$ and $5.4 \mu\text{g m}^{-3} \text{h}^{-1}$, respectively. The increase in the contribution from
787 heterogeneous chemistry was mainly attributed to the increase in relative humidity and
788 aerosol surfaces, upon which heterogeneous reactions took place. It is noticed that the
789 contribution of thermodynamic chemistry increased with increasing relative humidity as well
790 along with haze formation (Figure 8f). The increase in the contribution of thermodynamic
791 chemistry was remarkable (with IPR from 7.3 to $16 \mu\text{g m}^{-3} \text{h}^{-1}$), because gas precursors of
792 aerosols increased due to weakened vertical diffusivity and higher relative humidity during
793 haze period favored condensation from gas to aerosol phase. It is of interest that vertical
794 advection also contributed to $\text{PM}_{2.5}$ production (IPR of $5.4 \mu\text{g m}^{-3} \text{h}^{-1}$) in this stage, which
795 indicated a potential downward import of $\text{PM}_{2.5}$ from upper layer. It is also noticed that
796 horizontal advection contributed to $\text{PM}_{2.5}$ loss ($-12.8 \mu\text{g m}^{-3} \text{h}^{-1}$). This is because the strong
797 gradient between the increased $\text{PM}_{2.5}$ level in Beijing caused by weakened vertical diffusivity
798 and the relatively lower $\text{PM}_{2.5}$ level in the surrounding areas, which led to an outflow of
799 $\text{PM}_{2.5}$. In the growth stage, the net variation rate (IPR) of $\text{PM}_{2.5}$ concentration was $14.1 \mu\text{g}$
800 $\text{m}^{-3} \text{h}^{-1}$, in which emissions, chemical processes (GAS+Therm+HET) and physical processes
801 (HADV+VADV+HDIF+VDIF+DDEP) contributed $29.8 \mu\text{g m}^{-3} \text{h}^{-1}$, $33.5 \mu\text{g m}^{-3} \text{h}^{-1}$ and -49.2
802 $\mu\text{g m}^{-3} \text{h}^{-1}$, respectively. In the persistence stage, chemical production rate of $\text{PM}_{2.5}$ changed
803 slightly, and the production and loss rates of $\text{PM}_{2.5}$ were similar, leading to an approximately
804 zero IPR in this stage (Figure 8b). In the dissipation stage, the contribution of vertical
805 diffusion and dry deposition to $\text{PM}_{2.5}$ loss increased largely, while the total chemical



806 production rate decreased, which resulted in a net IPR of $-34.8 \mu\text{g m}^{-3} \text{h}^{-1}$, indicating a
807 substantial decrease in $\text{PM}_{2.5}$ concentration (Figure 8b). It was also noticed that HADV
808 contributed to $\text{PM}_{2.5}$ production in this stage, which was due to mass import to Beijing from
809 upwind areas by northwesterlies.

810 It should be mentioned that the contribution of emission was unchanged because the
811 monthly based emission inventory from MEIC was used, and the contribution of cloud
812 process was generally negligible throughout the period because there was little cloud and
813 precipitation during the study period.

814 We further use PA to interpret evolution processes of primary (BC) and secondary
815 (sulfate and nitrate) aerosols.

816 Black carbon is considered to be inert and chemical inactive, so it is governed solely by
817 physical processes. In the clean stage, BC production was contributed solely by emission (5.7
818 $\mu\text{g m}^{-3} \text{h}^{-1}$), whereas vertical diffusion and dry deposition contributed equally to BC loss (-2.7
819 $\mu\text{g m}^{-3} \text{h}^{-1}$), and other processes were negligible (Figure 8c). In the growth stage, the
820 contribution of vertical diffusion and dry deposition to BC loss decreased to $-2.0 \mu\text{g m}^{-3} \text{h}^{-1}$
821 and $-1.7 \mu\text{g m}^{-3} \text{h}^{-1}$, respectively, and the net rate of change was $0.7 \mu\text{g m}^{-3} \text{h}^{-1}$, indicating a
822 rapid increase of BC concentration in this stage (Figure 8c). In the persistence stage, the loss
823 rate by vertical diffusivity and dry deposition further increased mainly due to the increased
824 BC concentration (Figure 8c). It is noticed that horizontal advection somewhat contributed to
825 the loss of BC ($-0.7 \mu\text{g m}^{-3} \text{h}^{-1}$), which indicated an increasing outflow of BC to surrounding
826 areas. The IPR was near zero, indicating a balance of production and loss rate in this stage. In
827 the dissipation stage, BC loss via vertical diffusion and dry deposition processes increased
828 largely, mainly due to increasing wind speed and vertical diffusivity, and the net IPR became
829 $-1.6 \mu\text{g m}^{-3} \text{h}^{-1}$. This absolute value was larger than that in the growth stage ($0.7 \mu\text{g m}^{-3} \text{h}^{-1}$),
830 which indicated a faster decrease in BC concentration than the BC increase in the growth
831 stage (Figure 8c).

832 As for secondary aerosols, like sulfate, contribution from direct emission was near zero.
833 In the clean stage, gas chemistry ($5.9 \mu\text{g m}^{-3} \text{h}^{-1}$) was the predominant process for sulfate
834 production, and vertical diffusion contributed most to the loss ($-5.2 \mu\text{g m}^{-3} \text{h}^{-1}$) (Figure 8d). In
835 the growth stage, contribution from vertical diffusion was reduced to $-3.9 \mu\text{g m}^{-3} \text{h}^{-1}$ mainly



836 due to the decreased vertical diffusivity (Figure 8f), whereas positive contribution from gas
837 chemistry increased to $6.6 \mu\text{g m}^{-3} \text{h}^{-1}$, which was resulted from competitive processes. For
838 sulfate formation from gas chemistry ($\text{SO}_2 + \text{OH} \rightarrow \text{H}_2\text{SO}_4$), the oxidation of SO_2 to sulfate was
839 weakened because of decreasing OH radical due to increasing aerosol attenuation of solar
840 radiation, however, SO_2 increased due to weakened vertical diffusivity, leading to a slight net
841 increase of sulfate concentration compared with the clean stage. It is noteworthy that the
842 sulfate production rate from heterogeneous reactions increased to $2.7 \mu\text{g m}^{-3} \text{h}^{-1}$, mainly due
843 to the increases in SO_2 , aerosol surfaces and RH (as well as aerosol water content). All the
844 processes led to a net sulfate production rate of $2.7 \mu\text{g m}^{-3} \text{h}^{-1}$, in which chemistry played a
845 predominant role (IPR of $9.3 \mu\text{g m}^{-3} \text{h}^{-1}$). In the persistence stage, the contribution of gas and
846 heterogeneous processes further increased to $7.4 \mu\text{g m}^{-3} \text{h}^{-1}$ and $4.3 \mu\text{g m}^{-3} \text{h}^{-1}$, indicating an
847 increasing sulfate production through chemical processes (Figure 8d). It is interesting to note
848 that vertical diffusion contributed more to sulfate loss than in the growth stage, which was
849 mainly due to the higher sulfate level than in the growth stage while vertical diffusivity
850 coefficients were almost the same. The net IPR in this stage was just $0.2 \mu\text{g m}^{-3} \text{h}^{-1}$, which
851 indicated an approximate balance of production and loss. In the dissipation stage, increasing
852 vertical diffusivity was the dominant process for sulfate loss, and chemical contribution
853 decreased. It is noticed a positive contribution to sulfate from horizontal advection (IPR of
854 $4.3 \mu\text{g m}^{-3} \text{h}^{-1}$), which was due to an import of sulfate from upwind areas of Beijing by
855 northwesterly winds, like those for $\text{PM}_{2.5}$ and BC.

856 For nitrate, in the clean stage, thermodynamic process ($4.5 \mu\text{g m}^{-3} \text{h}^{-1}$) was the largest
857 contributor to nitrate production (Figure 8e). During the growth stage, the contribution of
858 thermodynamic processes ($10.2 \mu\text{g m}^{-3} \text{h}^{-1}$) increased by over a factor of two and was larger
859 than the contribution from heterogeneous process (Figure 8e). The substantial increase in the
860 contribution of thermodynamic processes to nitrate production was due to the combined
861 effects of the increased level of nitrate precursors (HNO_3 and NH_3) resulting from weakened
862 diffusivity and the increased RH favorable for gas to aerosol conversion. The contribution of
863 heterogeneous reactions increased as well due to the increased aerosol surface and relative
864 humidity. The net rate of nitrate change in this stage was $5.3 \mu\text{g m}^{-3} \text{h}^{-1}$. In the persistence
865 stage, the contribution from heterogeneous reactions changed slightly while the contribution



866 from thermodynamic process somewhat reduced (Figure 8e). This is because more NH_3 was
867 consumed to neutralize the increased sulfate, leaving less NH_3 to react with HNO_3 , and thus
868 producing fewer nitrate. The near zero net IPR of nitrate in this stage also indicated a balance
869 of production and loss. In the dissipating stage, the contribution of chemical processes was
870 almost the same as that in the clean stage, while physical processes dominated the loss and
871 the net IPR of nitrate (Figure 8e).

872

873 5.1.2 Haze evolution during 1-4 March

874 We also investigate another haze period of 1-4 March using PA (Figure 9). The hourly
875 IPRs by different processes are shown in Figure 9a. An apparent difference between this
876 episode and the first one was the positive IPRs of HADV during this episode, especially in
877 the growth stage from 21:00 (LST) on 1 March to 9:00 (LST) on 2 March, which indicated
878 that horizontal transport contributed to the haze formation. Another difference is that the
879 chemical processes, especially heterogeneous reactions contributed less to the $\text{PM}_{2.5}$ mass
880 during the persistence stage, such as from 10:00 (LST) on 2 March to 3:00 (LST) on 4 March,
881 which will be discussed below.

882 The IPRs for $\text{PM}_{2.5}$ and its components and meteorological variables averaged over each
883 stage during this episode are calculated and presented in Figure 9b to 9f. For BC (Figure 9c),
884 the most evident difference from the first haze episode occurred in the growth stage, in which
885 horizontal advection contributed $1.5 \mu\text{g m}^{-3} \text{h}^{-1}$ to BC production, which was comparable in
886 magnitude to the negative contributions from vertical diffusion and dry deposition ($-1.3 \mu\text{g}$
887 $\text{m}^{-3} \text{h}^{-1}$), suggesting the import of BC into Beijing from surrounding areas. The wind direction
888 in the south of Beijing at this stage was southerly and wind speed was about $2\text{-}3 \text{ m s}^{-1}$, so the
889 transport of pollutants from southern Hebei apparently contributed to the increase of BC level
890 in Beijing. Differently, during the first haze event on 20-26 February, wind direction was
891 easterly, bringing less polluted air mass from the Bohai Sea and northern Tianjin, so
892 horizontal advection contributed less to BC in Beijing. This transport feature was also
893 reflected in the change rates of sulfate (Figure 9d), nitrate (Figure 9e) and $\text{PM}_{2.5}$ (Figure 9b)
894 concentrations. An observational study for the same haze period in Beijing (Ma et al., 2017)
895 also suggested the important role of regional transport from the south of Beijing in haze



896 formation.

897 For sulfate (Figure 9d), although chemical processes still contributed most to sulfate
898 production in the growth stage ($6.0 \mu\text{g m}^{-3} \text{h}^{-1}$), it is noticed that gas chemistry ($5.9 \mu\text{g m}^{-3} \text{h}^{-1}$)
899 accounted for most of the sulfate production, whereas contribution from heterogeneous
900 reactions was smaller than that in the first haze episode mainly due to lower relative humidity.
901 In the growth stage, the net IPR was $1.9 \mu\text{g m}^{-3} \text{h}^{-1}$, 30% smaller than that for the first haze,
902 indicating a weaker secondary aerosol formation during this haze episode. In the persistence
903 stage, sulfate production from gas phase oxidation was almost balanced by the loss from dry
904 deposition and vertical diffusion, resulting in a net IRP of $-0.1 \mu\text{g m}^{-3} \text{h}^{-1}$, indicating a small
905 variation of sulfate concentration during this stage on average.

906 For nitrate, in the growth stage, it is of interest to note that heterogeneous reactions (5.5
907 $\mu\text{g m}^{-3} \text{h}^{-1}$) dominated over thermodynamic processes ($2.7 \mu\text{g m}^{-3} \text{h}^{-1}$) in nitrate formation,
908 which could be due to the low RH in this stage. Fountoukis and Nenes (2007) indicated that
909 nitrate aerosol is hardly formed in the ISORROPIA II model when RH is below 40%. The
910 average RH is about 37% during this haze episode, resulting in more nitrate formed by
911 heterogeneous reactions. The net IPR in the growth stage was $3.7 \mu\text{g m}^{-3} \text{h}^{-1}$, approximately
912 30% smaller than that in the first haze episode. In the persistence stage when relative
913 humidity increased to 51%, nitrate formation via thermodynamic processes became important,
914 and due to competition, nitrate formation from heterogeneous reactions was reduced.

915 For $\text{PM}_{2.5}$ (Figure 9b), in the growth stage, the IPR of $\text{PM}_{2.5}$ concentration was $13.0 \mu\text{g}$
916 $\text{m}^{-3} \text{h}^{-1}$, in which emission, chemical processes (GAS+Therm+HET) and physical processes
917 (HADV+VADV+HDIF+VDIF+DDEP) contributed $29.8 \mu\text{g m}^{-3} \text{h}^{-1}$, $23.9 \mu\text{g m}^{-3} \text{h}^{-1}$ and -40.7
918 $\mu\text{g m}^{-3} \text{h}^{-1}$, respectively. It is noteworthy that horizontal advection process (HADV)
919 contributed $22.4 \mu\text{g m}^{-3} \text{h}^{-1}$ to $\text{PM}_{2.5}$ production in this episode, which was comparable to the
920 total chemical production of $23.9 \mu\text{g m}^{-3} \text{h}^{-1}$. This reveals the comparable contributions to
921 $\text{PM}_{2.5}$ in Beijing from local sources and regional transport during this haze episode. In the
922 persistence stage, because of the change in wind direction and lower wind speed, the regional
923 transport of $\text{PM}_{2.5}$ became weak. The IPRs were $-4.0 \mu\text{g m}^{-3} \text{h}^{-1}$ for HADV and $1.2 \mu\text{g m}^{-3} \text{h}^{-1}$
924 for VADV, respectively, which were obviously smaller than those in the first haze episode. In
925 the dissipation stage, physical processes except HADV all contributed to the loss of $\text{PM}_{2.5}$.



926 Compared with the first haze episode, the negative IPR of VADV decreased mainly due to the
927 larger wind speeds in this episode, as more $PM_{2.5}$ was removed by VADV, the remaining
928 $PM_{2.5}$ loss by vertical diffusion decreased, consequently a weakened VDIF. The positive IPR
929 of HADV increased as well due to larger wind speed than that in the first episode in this
930 stage.

931 The above process analyses reveal that for the first haze episode (20-26 February) in
932 Beijing, local emissions and chemical processes were the main contributors to the formation
933 and persistence of the haze pollution. However, for the second haze (1-4 March), regional
934 transport or horizontal advection played a more important role in haze formation, with a
935 similar magnitude to local emissions and chemical productions in the growth stage. In all, for
936 both episodes, local emission, chemical reaction and horizontal advection were major
937 processes contributing to $PM_{2.5}$ increase, whereas vertical processes (diffusion, dry deposition
938 and advection) were major processes for $PM_{2.5}$ removal. As the pollution level increased, the
939 contribution of secondary aerosols through chemical formation to $PM_{2.5}$ increased apparently
940 in Beijing.

941

942 5.2 Contributions of physical and chemical processes to the aerosol feedback

943 5.2.1 The first haze episode (20-26 February)

944 Figure 10 shows the contributions of each process to the feedback-induced difference in
945 the change rates of $PM_{2.5}$ and its major components (ΔIPR) during the first haze episode
946 (20-26 February), which were derived from the difference between cases with and without
947 aerosol radiative effects (FULL minus NoAer).

948 The definition of the four stages during haze evolution is the same as that in section 5.1.1.
949 For BC (Figure 10b) in the clean stage, the aerosol feedback caused a decrease in vertical
950 diffusion and advection (Figure 10e), leading to an increase in BC concentration with the
951 ΔIPR of $0.40 \mu\text{g m}^{-3} \text{h}^{-1}$ from VDIF+VADV, concurrently, the feedback caused an increased
952 loss of BC through horizontal diffusion (HDIF) and advection (HADV) and dry deposition
953 (DDEP) due to the increased BC concentration, with the ΔIPR of $-0.39 \mu\text{g m}^{-3} \text{h}^{-1}$ from
954 HADV+HDIF+DDEP (Figure 10b). The net ΔIPR was near zero, which indicated a
955 negligible feedback effect during the clean stage. In the growth stage, the feedback caused a



956 pronounced decrease in vertical diffusivity, advection, as well as dry deposition velocity,
957 leading to apparent increases in BC level, with the contributions to Δ IPRs from VDIF, VADV,
958 and DDEP being $0.50 \mu\text{g m}^{-3} \text{h}^{-1}$, $0.50 \mu\text{g m}^{-3} \text{h}^{-1}$ and $0.20 \mu\text{g m}^{-3} \text{h}^{-1}$, respectively (Figure
959 10b). The increase in BC concentration consequently led to an increase in outflow via HADV
960 and HDIF, with the Δ IPRs of $-0.63 \mu\text{g m}^{-3} \text{h}^{-1}$ and $-0.12 \mu\text{g m}^{-3} \text{h}^{-1}$, respectively, which tended
961 to reduce BC concentration. The total effect by summing the processes exhibited a net
962 positive Δ IPR of $0.44 \mu\text{g m}^{-3} \text{h}^{-1}$, which indicated an apparent increase in BC concentration
963 due to the feedback. In the persistence stage, the sign of Δ IPR for each process was the same
964 as that in the growth stage, and the Δ IPR by vertical processes ($0.84 \mu\text{g m}^{-3} \text{h}^{-1}$ from
965 VADV+VDIF+DDEP) was generally balanced by that of horizontal processes ($-0.80 \mu\text{g m}^{-3}$
966 h^{-1} from HADV+HDIF) and led to a net Δ IPR of $0.04 \mu\text{g m}^{-3} \text{h}^{-1}$ (Figure 10b), which
967 indicated the difference in the BC change rate between the FULL and NoAer cases was small
968 in this stage. In the dissipating stage, the Δ IPRs were negative for all the processes except for
969 HADV. This was because of the higher BC levels due to the feedback, which caused more
970 BC to be removed than without feedback, although the vertical diffusion coefficient was
971 smaller due to the feedback. The positive Δ IPR from HADV suggested the enhanced BC
972 import into Beijing from upwind regions due to the feedback. The sum of these processes
973 produced a net Δ IPR of $-1.20 \mu\text{g m}^{-3} \text{h}^{-1}$, which indicated a larger decreasing rate of BC
974 concentration (from haze to clean level) due to aerosol feedback in this stage.

975 For sulfate (Figure 10c), in the clean stage, the feedback-induced changes were as small
976 as those for BC. In the growth stage, besides the positive Δ IPRs by VDIF, VADV and DDEP
977 as those for BC, the most impressive feature was the larger contributions from GAS and HET,
978 with the Δ IPRs being $0.29 \mu\text{g m}^{-3} \text{h}^{-1}$ and $1.73 \mu\text{g m}^{-3} \text{h}^{-1}$, respectively, much larger than those
979 ($0.11 \mu\text{g m}^{-3} \text{h}^{-1}$ and $0.23 \mu\text{g m}^{-3} \text{h}^{-1}$) in the clean stage because of the increased gas
980 precursors, aerosol surfaces and RH due to the feedback effect, which enhanced chemical
981 formation (Figure 10c, 10e). The sum of the Δ IPRs by all the processes was $1.92 \mu\text{g m}^{-3} \text{h}^{-1}$,
982 indicating an apparent increase in sulfate concentration due to the feedback effect. In the
983 persistence stage, the Δ IPRs by GAS and HET increased. However, the Δ IPR of VDIF
984 became negative, which could be explained by the increased sulfate concentration due to
985 aerosol feedback caused more sulfate to be removed through vertical diffusion, leading to a



986 negative Δ IPR of VDIF, although the vertical diffusion coefficient was reduced by the
987 feedback. In the dissipation stage, the Δ IPR by HET decreased because the feedback-induced
988 differences in the concentrations of precursors and aerosols became smaller. The large
989 negative Δ IPR by VDIF indicated a larger decreasing rate in sulfate concentration from the
990 persistence to clean stages due to the feedback.

991 For nitrate (Figure 10d), the feedback-induced IPR changes in the clean stage were
992 similar to those for sulfate. In the growth stage, remarkable increases in nitrate formation
993 from Thermo and HET processes occurred, with the Δ IPRs of $3.30 \mu\text{g m}^{-3} \text{h}^{-1}$ and $0.50 \mu\text{g m}^{-3}$
994 h^{-1} , respectively (Figure 10d). The increased gas precursors and RH due to the aerosol
995 feedback reinforced chemical formation processes. In this stage, the overall Δ IPR was 3.90
996 $\mu\text{g m}^{-3} \text{h}^{-1}$, suggesting a faster increasing rate in nitrate concentration in consideration of
997 aerosol feedback. In the persistence stage, the Δ IPR by Thermo was smaller than that in the
998 growth stage (Figure 10d). This could be explained that the apparent increase in sulfate
999 concentration via HET and GAS due to the feedback (Figure 10c) in this stage consumed
1000 more ammonia, which inhibited the formation of nitrate ammonium via thermodynamic
1001 processes. The net Δ IPR by all the processes in this stage was near zero, which indicated that
1002 the radiative feedback exerted little effect on the change rate of nitrate concentration during
1003 this stage. In the dissipation stage, the attenuation of solar radiation by aerosols was
1004 weakened because of the decrease in aerosol concentration, meanwhile, the concentrations of
1005 gas precursors (NO_x) were elevated due to the feedback, the combined effect resulted in an
1006 increase of photochemical production of HNO_3 ; in addition, RH was increased due to the
1007 feedback as well, as a result, nitrate formation via thermodynamic process was enhanced,
1008 leading to a positive Δ IPR of $3.73 \mu\text{g m}^{-3} \text{h}^{-1}$ by Thermo in this stage.

1009 For $\text{PM}_{2.5}$, the net Δ IPR due to aerosol feedback in the clean stage was $0.30 \mu\text{g m}^{-3} \text{h}^{-1}$, in
1010 which $1.22 \mu\text{g m}^{-3} \text{h}^{-1}$ was from chemical processes (GAS+Thermo+HET) and $-0.90 \mu\text{g m}^{-3}$
1011 h^{-1} from physical processes (HADV+VADV+HDIF+VDIF+DDEP) (Figure 10a). In the
1012 growth stage, the net Δ IPR was $9.50 \mu\text{g m}^{-3} \text{h}^{-1}$, which meant in every hour, approximate 9.50
1013 $\mu\text{g m}^{-3}$ of $\text{PM}_{2.5}$ mass was elevated in Beijing due to the feedback effect. The above
1014 feedback-induced difference in the change rate of $\text{PM}_{2.5}$ (Δ IPR) resulted from a combined
1015 effect from chemical processes ($7.27 \mu\text{g m}^{-3} \text{h}^{-1}$) and physical processes ($2.23 \mu\text{g m}^{-3} \text{h}^{-1}$),



1016 which suggested that chemical processes contributed more to the $PM_{2.5}$ increase than physical
1017 processes. However, it was noted that the increased contribution from chemical processes
1018 was related to increasing gas precursors, which was partly associated with physical processes.
1019 It was noteworthy that the positive $\Delta IPRs$ were contributed by both chemical processes (GAS,
1020 Thermo and HET) and vertical movements (VADV, VDIF and DDEP) (Figure 10a). The sum
1021 of positive $\Delta IPRs$ was $22.88 \mu\text{g m}^{-3} \text{h}^{-1}$, in which $7.27 \mu\text{g m}^{-3} \text{h}^{-1}$ was from chemical
1022 processes and $15.61 \mu\text{g m}^{-3} \text{h}^{-1}$ from vertical movements. This suggested a larger
1023 feedback-induced $PM_{2.5}$ increase through vertical movements than via chemical processes.
1024 However, the outflow (HADV+HDIF) of $PM_{2.5}$ was also enhanced due to the increased $PM_{2.5}$
1025 level by aerosol feedback, producing a negative ΔIPR ($-13.38 \mu\text{g m}^{-3} \text{h}^{-1}$), and partly
1026 offsetting the positive ΔIPR ($15.61 \mu\text{g m}^{-3} \text{h}^{-1}$) by vertical movements, resulting in a net ΔIPR
1027 of $2.23 \mu\text{g m}^{-3} \text{h}^{-1}$ from all the physical processes. In the persistence stage, the sign of $\Delta IPRs$
1028 by different processes generally resembled those in the growth stage except that of VDIF
1029 whose ΔIPR was negative, which indicated more removal though VDIF mainly due to the
1030 increased secondary aerosol concentrations by aerosol feedback. The net ΔIPR by all the
1031 processes was $0.40 \mu\text{g m}^{-3} \text{h}^{-1}$ in this stage, indicating a small influence of aerosol feedback
1032 on the change rate of $PM_{2.5}$ concentration. In the dissipating stage (Figure 10a), the large
1033 negative ΔIPR from VDIF indicated more $PM_{2.5}$ mass was removed via vertical diffusion
1034 while considering aerosol feedback, although the feedback induced a smaller vertical
1035 diffusivity coefficient. The net ΔIPR of $-24.60 \mu\text{g m}^{-3} \text{h}^{-1}$ indicated a larger decreasing rate of
1036 $PM_{2.5}$ concentration in the FULL case than in the NoAer case.

1037

1038 5.2.2 The second haze episode (1-4 March)

1039 For BC in the second haze episode (1-4 March), the most obvious difference from the
1040 first episode was in the growth stage, in which the ΔIPR by horizontal advection (HADV)
1041 was $0.70 \mu\text{g m}^{-3} \text{h}^{-1}$ (Figure 11b). The radiative feedback led to a weakened vertical
1042 diffusivity and a decreased PBL height (Figure 11e), which favored the accumulation of BC
1043 and caused a positive ΔIPR of $0.40 \mu\text{g m}^{-3} \text{h}^{-1}$ from VDIF. The wind direction in the growth
1044 stage was southerlies as discussed above, bringing aerosols from the south to Beijing. The
1045 aerosol feedback enhanced BC concentration in source regions through reducing vertical



1046 diffusivity, leading to an increased northward flux of BC and a positive Δ IPR from HADV.
1047 The higher BC concentration due to the feedback via HADV and VDIF consequently led to
1048 an increase in BC outflow out of Beijing via vertical advection (VADV) and horizontal
1049 diffusion (HDIF), with the Δ IPRs of $-0.60 \mu\text{g m}^{-3} \text{h}^{-1}$ and $-0.20 \mu\text{g m}^{-3} \text{h}^{-1}$, respectively. In this
1050 stage, the net Δ IPR of BC was $0.20 \mu\text{g m}^{-3} \text{h}^{-1}$, in which $0.50 \mu\text{g m}^{-3} \text{h}^{-1}$ was from horizontal
1051 movements (HADV+HDIF) and $-0.30 \mu\text{g m}^{-3} \text{h}^{-1}$ from vertical movements
1052 (VADV+VDIF+DDEP), indicating that the feedback effect strengthened the contribution of
1053 horizontal movements to surface BC concentration in Beijing. In the persistence stage (Figure
1054 11b), the net Δ IPR was also near zero ($-0.02 \mu\text{g m}^{-3} \text{h}^{-1}$), indicating that the BC change rate
1055 was merely affected by the feedback in this stage. In the dissipation stage (Figure 11b), the
1056 Δ IPRs were negative for all the processes except for VDIF. This could be attributed to the
1057 higher BC levels due to the feedback, which caused more BC to be removed than without
1058 feedback through these processes. The net Δ IPR was $-0.17 \mu\text{g m}^{-3} \text{h}^{-1}$, the same as that in the
1059 growth stage, but with opposite sign.

1060 For sulfate (Figure 11c), in the growth stage, different from the relatively large positive
1061 Δ IPR by chemical processes in the first haze episode, the feedback caused small IPR changes
1062 via chemical production because SO_2 concentration in this episode was lower than that in the
1063 first one and sulfate was mainly formed in upwind regions and transported to Beijing.
1064 Consequently, relatively large sulfate increases through HADV and VDIF in this episode. In
1065 this stage, the feedback caused a slight increase in sulfate concentration by GAS with Δ IPR
1066 of $0.17 \mu\text{g m}^{-3} \text{h}^{-1}$ due to slightly elevated precursors, however, because of the low relative
1067 humidity (mean RH was 38%) and competitive processes, heterogeneous reactions were
1068 depressed. In terms of physical processes, due to the feedback effect, horizontal transport
1069 (HADV) was strengthened (Δ IPR of $1.0 \mu\text{g m}^{-3} \text{h}^{-1}$) due to the increased sulfate concentration
1070 to the south of Beijing, meanwhile, the weakened vertical diffusivity caused an increase in
1071 sulfate concentration by VDIF and DDEP, with the Δ IPRs of $1.0 \mu\text{g m}^{-3} \text{h}^{-1}$ and $0.57 \mu\text{g m}^{-3}$
1072 h^{-1} , respectively, consequently, the outflow of sulfate out of Beijing was also increased via
1073 vertical advection (VADV) and horizontal diffusion (HDIF). The net Δ IPR in the growth
1074 stage was $0.90 \mu\text{g m}^{-3} \text{h}^{-1}$, indicating an apparent increase in sulfate concentration due to the
1075 feedback. In the persistence stage, the Δ IPRs by GAS and HET changed slightly compared



1076 with those in the growth stage. The negative ΔIPR by VDIF indicated more loss of sulfate by
1077 vertical diffusion while considering aerosol feedback. The net ΔIPR in this stage was $0.02 \mu\text{g}$
1078 $\text{m}^{-3} \text{h}^{-1}$, indicating a negligible feedback effect on sulfate change rate in this stage. In the
1079 dissipation stage, the feedback-induced higher sulfate concentration caused more removal of
1080 sulfate via physical processes except HADV, resulting in a net ΔIPR of $-0.64 \mu\text{g} \text{m}^{-3} \text{h}^{-1}$. The
1081 positive ΔIPR from HADV was due to the strengthened import from upwind areas due to the
1082 feedback.

1083 For nitrate, in the growth stage, the feedback also induced an increase in nitrate
1084 concentration via horizontal advection like sulfate (Figure 11d). The increases in gas
1085 precursors and aerosol surfaces due to the feedback enhanced nitrate formation, resulting in
1086 nitrate increases via Thermo and HET, with the ΔIPRs of $0.88 \mu\text{g} \text{m}^{-3} \text{h}^{-1}$ and $0.46 \mu\text{g} \text{m}^{-3} \text{h}^{-1}$,
1087 respectively. To the persistence stage, the chemical production of nitrate increased largely
1088 caused by the feedback, with the ΔIPR of Thermo being $4.30 \mu\text{g} \text{m}^{-3} \text{h}^{-1}$. The reason could be
1089 the low RH in the growth stage (38% shown in Figure 9f) left most of nitric acid remained in
1090 gas phase together with the increase in RH due to the feedback (13.2% shown in Figure 11e)
1091 drove its conversion from gas to aerosol phase. Due to the enhanced thermodynamics
1092 production, nitrate formation via heterogeneous reactions was depressed in this stage. The
1093 increased nitrate concentration via Thermo led to larger removal via vertical diffusion,
1094 resulting in a negative ΔIPR of $-4.80 \mu\text{g} \text{m}^{-3} \text{h}^{-1}$ by VDIF, and a net ΔIPR of $-0.10 \mu\text{g} \text{m}^{-3} \text{h}^{-1}$.
1095 In the dissipation stage, like that in the first haze episode, the reduced aerosol attenuation of
1096 solar radiation and increased RH induced by aerosol feedback led to an increase in nitrate via
1097 thermodynamic process, with the ΔIPR of $1.80 \mu\text{g} \text{m}^{-3} \text{h}^{-1}$ by Thermo. Consequently,
1098 heterogeneous reactions were depressed due to competitive processes (ΔIPR of $-0.97 \mu\text{g} \text{m}^{-3}$
1099 h^{-1} by HET). In this stage, because of the higher nitrate concentration, the feedback led to
1100 larger removal by vertical processes (the ΔIPR of VADV+VDIF+DDEP was $-3.23 \mu\text{g} \text{m}^{-3} \text{h}^{-1}$),
1101 with a net ΔIPR of $-1.78 \mu\text{g} \text{m}^{-3} \text{h}^{-1}$, similar to the ΔIPR in the growth stage but with opposite
1102 sign.

1103 For $\text{PM}_{2.5}$ (Figure 11a), the net ΔIPR due to aerosol feedback in the growth stage was
1104 $2.40 \mu\text{g} \text{m}^{-3} \text{h}^{-1}$, with $1.40 \mu\text{g} \text{m}^{-3} \text{h}^{-1}$ from physical processes
1105 (HADV+VADV+HDIF+VDIF+DDEP) and $1.0 \mu\text{g} \text{m}^{-3} \text{h}^{-1}$ from chemical processes



1106 (GAS+Thermo+HET), which indicated that the feedback-induced increase in PM_{2.5}
1107 concentration per hour was produced through larger contributions from physical processes
1108 than chemical processes in this episode. HADV contributed most to the PM_{2.5} increase (with
1109 ΔIPR of 10.20 μg m⁻³ h⁻¹), followed by VDIF (with ΔIPR of 2.90 μg m⁻³ h⁻¹). As mentioned
1110 above, the weakened vertical diffusivity caused by the feedback enhanced aerosol
1111 concentrations in the entire BTH region, meanwhile, the feedback induced a southeast wind
1112 anomaly with a slight change in wind speed in the regions south of Beijing. The combined
1113 effect of the elevated aerosol concentrations and southeast wind anomaly brought more
1114 aerosols to Beijing. In the persistence stage, the feedback increased PM_{2.5} concentration
1115 mainly through chemical processes, with the ΔIPR of 6.05 μg m⁻³ h⁻¹, which was mainly
1116 resulted from the enhanced thermodynamic production of ammonium nitrate, and such
1117 increase in aerosol mass due to feedback led to more aerosols to be diffused than that without
1118 feedback, leading to the ΔIPR of -7.30 μg m⁻³ h⁻¹ by VDIF. It is noticed that the signs of the
1119 ΔIPRs by VDIF were opposite between the growth and persistence stages even though the
1120 vertical diffusivities were both decreased. In the growth stage, the PM_{2.5} concentration was
1121 gradually increasing, the effect of the weakened vertical diffusivity was dominated, resulting
1122 in a positive ΔIPR by VDIF which favored further accumulation of aerosols; in the
1123 persistence stage, the aerosol concentration had already been elevated to a high level, the
1124 effect of higher concentration surpassed that of weakened vertical diffusivity due to the
1125 feedback and led to a negative ΔIPR, which meant the feedback caused more loss of PM_{2.5}
1126 via VDIF. In the persistence stage, the net ΔIPR was 0.44 μg m⁻³ h⁻¹, in which -5.6 μg m⁻³ h⁻¹
1127 from physical processes and 6.05 μg m⁻³ h⁻¹ from chemical processes, which indicated the
1128 feedback-induced overall changes in the change rate of PM_{2.5} concentration in this stage were
1129 relatively small. In the dissipating stage, the removal of PM_{2.5} was enhanced by the feedback
1130 through all the processes except HADV mainly due to the increased PM_{2.5} concentration, the
1131 positive ΔIPR by HADV was caused by the enhanced import from upwind areas due to the
1132 feedback. In this stage, the feedback effect enhanced the removal of PM_{2.5}, which was
1133 reflected by the net negative ΔIPR of -4.30 μg m⁻³ h⁻¹.

1134 The above analyses quantify the key processes contributing to the aerosol radiative
1135 feedback in Beijing during the two haze episodes. In the growth stage of the first haze



1136 episode, the feedback-induced $PM_{2.5}$ enhancement was attributed to the positive contributions
1137 from chemical processes and vertical movements, but partly offset by the increased outflow
1138 of $PM_{2.5}$ via horizontal advection, resulting in a larger increase in $PM_{2.5}$ through chemical
1139 processes than that from physical processes. Differently, during the second haze episode, the
1140 feedback-induced $PM_{2.5}$ enhancement in the growth stage was larger by physical processes
1141 than that by chemical processes, and horizontal advection contributed most to the $PM_{2.5}$
1142 enhancement. In all, the radiative feedback increased the cumulative rate of aerosols in the
1143 growth stage via promoting chemical formations, weakening vertical diffusions and/or
1144 enhancing regional transport by horizontal advection. For both episodes, the radiative
1145 feedback exerted small effect on the change rate of $PM_{2.5}$ concentration during the persistence
1146 stage and reinforced the decreasing rate of $PM_{2.5}$ in the dissipation stage.

1147

1148 **6 Conclusion**

1149 Several severe haze events occurred in the winter of 2014, with the most severe one on
1150 20-26 February. An online-coupled regional atmospheric chemistry/aerosol-climate model
1151 (RIEMS-Chem) was developed and utilized to investigate the mechanisms of haze formation
1152 and aerosol radiative feedback in the Beijing-Tianjin-Hebei (BTH) region. The heterogeneous
1153 chemical reactions were treated in the model and the measured size distribution and mixing
1154 state of aerosols in Beijing were used to constrain the model. Two numerical experiments,
1155 with and without aerosol effects were conducted to explore the aerosol radiative effects
1156 (AREs) and feedbacks on meteorological fields and aerosol distributions. Processes analysis
1157 technique was implemented in RIEMS-Chem to quantify the individual contributions from
1158 various physical and chemical processes to aerosol evolution and radiative feedback. Model
1159 performance was comprehensively evaluated by comparing with a variety of observations for
1160 meteorological variables, surface shortwave radiation, PBL heights, $PM_{2.5}$ and its chemical
1161 components, as well as aerosol optical properties in the BTH region. The comparisons
1162 demonstrated that RIEMS-Chem was able to represent the magnitudes and variations of the
1163 above variables reasonably well, in particular, improving the simulation of inorganic aerosols
1164 and AOD, which was often underpredicted in current on-line coupled models. It is



1165 encouraging that by considering the aerosol radiative effects, the model apparently improved
1166 predictions for meteorological variables, $PM_{2.5}$ and its chemical compositions and aerosol
1167 optical properties in the BTH region, suggesting the importance and necessity for developing
1168 chemistry-climate online coupled models in both air quality and climate research.

1169 During the study period, the meteorological conditions were characterized by weak
1170 southerly winds, high RH and low PBL height, which favored aerosol accumulation and haze
1171 formation in the BTH region. The average T2, WS10, RH2, PBL height and $PM_{2.5}$
1172 concentration from the FULL case were simulated to be $0.6\text{ }^{\circ}\text{C}$, 1.2 m s^{-1} , 67.0%, 698.4 m
1173 and $90.0\text{ }\mu\text{g m}^{-3}$, respectively, over the BTH region during the study period.

1174 The distribution pattern of AOD generally resembled that of $PM_{2.5}$, with the domain
1175 mean value of 0.78 and the maximum up to 1.1 during the study period. It was noteworthy
1176 that the simulated SSA averaged over the BTH region and the study period was 0.91, which
1177 indicated the dominance of scattering aerosols. The domain and period average AREs at the
1178 surface, in the atmosphere and at the TOA were estimated to be -37 W m^{-2} , 19 W m^{-2} and -18
1179 W m^{-2} , respectively, and they were enhanced to -57 W m^{-2} , 25 W m^{-2} and -32 W m^{-2} during
1180 the most severe haze episode (20-26 February). It was striking that the maximum hourly
1181 AREs at the surface and at TOA reached -384 W m^{-2} and -231 W m^{-2} around noon time in the
1182 vicinity of Shijiazhuang during the first haze episode. The magnitude of the model simulated
1183 AREs during the haze episode in this study agreed favorably with previous observational
1184 based estimates.

1185 The aerosol radiative effects generally led to a reduction in surface air temperature in the
1186 entire domain with larger decrease in southern BTH ($-1.2\text{ }^{\circ}\text{C} \sim -2\text{ }^{\circ}\text{C}$), accompanied by an
1187 increase in RH2 (10% \sim 16%) and a decrease in PBL height ($-240\text{ m} \sim -210\text{ m}$). The changes
1188 in these meteorological variables were strengthened during the severe haze episode.
1189 Noticeably, $PM_{2.5}$ concentrations were consistently increased over the BTH region due to the
1190 aerosol feedback, with the maximum average increase exceeding $33\text{ }\mu\text{g m}^{-3}$ (33%) in southern
1191 Hebei and portions of Beijing and Tianjin during the study period, and the maximum hourly
1192 increase was up to $372\text{ }\mu\text{g m}^{-3}$ (186%) in the vicinity of Shijiazhuang during the severe haze
1193 episode. In terms of domain and period average, the feedback-induced changes were $-1.4\text{ }^{\circ}\text{C}$
1194 for T2, -0.04 m s^{-1} for WS10, 8.7% for RH2, $-3.3\text{ m}^2\text{ s}^{-1}$ for vertical diffusion coefficient,



1195 -160.0 m (-19%) for PBL height and $20.0 \mu\text{g m}^{-3}$ (29%) for $\text{PM}_{2.5}$ concentration. The
1196 magnitude of the above changes were enhanced during the severe haze episode, with the
1197 7-day mean changes in T2, WS10, RH2, PBL height and $\text{PM}_{2.5}$ concentration being $-1.8 \text{ }^\circ\text{C}$,
1198 -0.5 m s^{-1} , 9.8%, -183.6 m (-31%) and $45.1 \mu\text{g m}^{-3}$ (39%), respectively, which demonstrated
1199 the significant aerosol radiative feedback on $\text{PM}_{2.5}$ accumulation and haze formation. The
1200 changes in sulfate and nitrate concentrations were larger than that in BC concentration
1201 because secondary aerosols were increased not only by weakened vertical diffusivity but also
1202 by enhanced chemical reactions caused by the feedback.

1203 The magnitude of the feedback effect varied remarkably during haze evolution. The
1204 absolute change in $\text{PM}_{2.5}$ concentration caused by the feedback was largest in the persistence
1205 stage, followed by those in the growth stage and in the dissipating stage. In Beijing, the
1206 feedback-induced increases in $\text{PM}_{2.5}$ concentration were $55 \mu\text{g m}^{-3}$, $84 \mu\text{g m}^{-3}$, $40 \mu\text{g m}^{-3}$,
1207 respectively, during the growth, persistence and dissipation stages of the severe haze episode.

1208 PA method was applied to calculate the IPRs for quantifying the individual contributions
1209 from physical and chemical processes to variations of $\text{PM}_{2.5}$ and its chemical components
1210 during haze episodes in Beijing. Two haze episodes were analyzed and compared to elucidate
1211 the mechanism of haze formation and evolution. For the first haze episode, the net IPR for
1212 $\text{PM}_{2.5}$ was $14.1 \mu\text{g m}^{-3} \text{ h}^{-1}$ in the growth stage, in which emissions, chemical processes and
1213 physical processes contributed $29.8 \mu\text{g m}^{-3} \text{ h}^{-1}$, $33.5 \mu\text{g m}^{-3} \text{ h}^{-1}$ and $-49.2 \mu\text{g m}^{-3} \text{ h}^{-1}$,
1214 respectively, which indicated a remarkable $\text{PM}_{2.5}$ increase contributed by chemical processes
1215 in this stage. The most influential processes for $\text{PM}_{2.5}$ loss and production were vertical
1216 diffusion and thermodynamic processes, respectively. Compared with the clean stage, the
1217 losses by vertical diffusion and dry deposition reduced largely, and the production by
1218 chemical processes increased, both leading to an evident increase in surface $\text{PM}_{2.5}$
1219 concentrations in the growth stage. In the persistence stage, the production and loss of $\text{PM}_{2.5}$
1220 were almost equal, resulting in an approximately zero IPR in this stage. In the dissipation
1221 stage, the loss of $\text{PM}_{2.5}$ by vertical diffusion and dry deposition increased greatly, leading to a
1222 net IPR rate of $-34.8 \mu\text{g m}^{-3} \text{ h}^{-1}$, which meant a substantial decrease in $\text{PM}_{2.5}$ concentration.

1223 For the second haze episode, the net IPR for $\text{PM}_{2.5}$ was $13.0 \mu\text{g m}^{-3} \text{ h}^{-1}$ in the growth
1224 stage, in which emissions, chemical processes and physical processes contributed $29.8 \mu\text{g m}^{-3}$



1225 h^{-1} , $23.9 \mu\text{g m}^{-3} \text{h}^{-1}$ and $-40.8 \mu\text{g m}^{-3} \text{h}^{-1}$, respectively. It was noteworthy that the contribution
1226 of horizontal advection to $\text{PM}_{2.5}$ was of a similar magnitude to the contributions from local
1227 emissions and chemical processes, with the mean IPR of $22.4 \mu\text{g m}^{-3} \text{h}^{-1}$, which indicated the
1228 important contribution of regional transport to haze formation in Beijing. Process analysis for
1229 the changes in $\text{PM}_{2.5}$ components during haze evolution was also conducted.

1230 The contribution of each physical and chemical process to the feedback-induced changes
1231 in $\text{PM}_{2.5}$ and its major components were explored and quantified. For the first haze episode,
1232 the fast increase in $\text{PM}_{2.5}$ (ΔIPR of $9.5 \mu\text{g m}^{-3} \text{h}^{-1}$) due to aerosol feedback in the growth stage
1233 was mainly attributed to the changes in vertical movements (VDIF and VADV) and chemical
1234 processes, but the increased outflow via horizontal advection (HADV) partly offset the
1235 increased $\text{PM}_{2.5}$ due to vertical movements, which caused a larger contribution to the $\text{PM}_{2.5}$
1236 increase from chemical processes (ΔIPR of $7.27 \mu\text{g m}^{-3} \text{h}^{-1}$) than that from physical processes
1237 (ΔIPR $2.23 \mu\text{g m}^{-3} \text{h}^{-1}$). However, during the second haze episode, the feedback-induced
1238 $\text{PM}_{2.5}$ increase (ΔIPR of $2.4 \mu\text{g m}^{-3} \text{h}^{-1}$) in the growth stage was mainly contributed by
1239 physical processes (ΔIPR of $1.40 \mu\text{g m}^{-3} \text{h}^{-1}$) rather than that by chemical processes (ΔIPR of
1240 $1.0 \mu\text{g m}^{-3} \text{h}^{-1}$), and among physical processes, the $\text{PM}_{2.5}$ increase was mainly attributed to the
1241 increased horizontal advection (ΔIPR of $10.2 \mu\text{g m}^{-3} \text{h}^{-1}$). In general, in the growth stage of
1242 haze episodes, the feedback increased the accumulation rate of aerosols mainly through
1243 enhancing chemical formations, weakening vertical diffusions and/or enhancing regional
1244 transport by advectations. The feedback-induced changes in the change rate of $\text{PM}_{2.5}$
1245 concentration were small during the persistence stage, and the feedback enhanced the
1246 removal rate of $\text{PM}_{2.5}$ in the dissipation stage mainly through increasing vertical diffusion
1247 and/or vertical advection.

1248 The results from this study demonstrated a significant impact of aerosol radiative
1249 feedback on meteorology, chemistry, aerosol distribution and evolution during winter haze
1250 events in the BTH region. The mechanism and processes through which the feedback affected
1251 haze formation and evolution were elucidated and quantified. More cases in different regions,
1252 seasons and years are needed to investigate the feedback mechanism at different scales and in
1253 more details. This study also pointed out the significance and necessity of developing online
1254 coupled model for exploring chemistry/aerosol-weather/climate interactions and for



1255 improving meteorological and chemical predictions in both air quality and climate research in
1256 the future.

1257

1258 **Author Contributions**

1259 ZH designed the study, JL performed the model simulation, JL and ZH processed and
1260 analyzed the modeling data, ZH and JL wrote the paper, JL and ZX contributed to the model
1261 development, YW provided and analyzed the chemical observation data, XX provided the
1262 meteorological sounding and aerosol optical observation data, JL and LL processed and
1263 analyzed the observational data, RZ synthesized and analyzed the observation.

1264

1265 **Data availability.**

1266 The observational data can be accessed through contacting the corresponding authors.

1267

1268 **Competing interests.**

1269 The authors declare that they have no conflict of interests.

1270

1271 **Special issue statement.**

1272 This article is part of the special issue “Regional assessment of air pollution and climate
1273 change over East and Southeast Asia: results from MICS-Asia Phase III”. It is not associated
1274 with a conference.

1275

1276 **Acknowledgement.**

1277 This study was supported by the National Natural Science Foundation of China (no.
1278 91644217), the National Key R&D Program of China (2019YFA0606802) and the Jiangsu
1279 Collaborative Innovation Center for Climate Change.

1280

1281 **References**

- 1282 Albrecht, B.: Aerosols, cloud microphysics, and fractional cloudiness, *Science*, 245, 1227,
1283 <https://doi.org/10.1126/science.245.4923.1227>, 1989.
- 1284 An, Z., Huang, R., Zhang, R., Tie, X., Li, G., Cao, J., Zhou, W., Shi, Z., Han, Y., Gu, Z., and
1285 Ji, Y.: Severe haze in northern China: A synergy of anthropogenic emissions and
1286 atmospheric processes, *P. Natl. Acad. Sci. USA*, 116,18, 8657–8666, 2019.
- 1287 Baklanov, A., Schlunzen, K., Suppan, P., Baldasano, J., Brunner, D., Aksoyoglu, S.,
1288 Carmichael, G., Douros, J., Flemming, J., Forkel, R., Galmarini, S., Gauss, M., Grell, G.,
1289 Hirtl, M., Joffre, S., Jorba, O., Kaas, E., Kaasik, M., Kallos, G., Kong, X., Korsholm, U.,



- 1290 Kurganskiy, A., Kushta, J., Lohmann, U., Mahura, A., Manders-Groot, A., Murizi, A.,
1291 Moussiopoulos, N., Rao, S.T., Savage, N., Seigneur, C., Sokhi, R.S., Solazzo, E.,
1292 Solomos, S., Sorenson, B., Tsegas, G., Vignati, E., Vogel, B., and Zhang, Y.: Online
1293 coupled regional meteorology chemistry models in Europe: current status and prospects,
1294 *Atmos. Chem. Phys.*, 14, 317-398, doi:10.5194/acp-14-317-2014, 2014.
- 1295 Cai, W., Li, K., Liao, H., Wang, H., and Wu, L.: Weather conditions conducive to Beijing
1296 severe haze more frequent under climate change, *Nature Clim. Change*, 7, 257–262, doi:
1297 10.1038/nclimate3249, 2017.
- 1298 Carslaw, K. S., Boucher, O., Spracklen, D. V., Mann, G. W., Rae, J. G. L., Woodward, S., and
1299 Kulmala, M.: A review of natural aerosol interactions and feedbacks within the Earth
1300 system, *Atmos. Chem. Phys.*, 10, 1701–1737, doi:10.5194/acp-10-1701-2010, 2010.
- 1301 Chan, C. and Yao, X.: Air pollution in megacities in China, *Atmos. Environ.*, 42, 1-42, 2008.
- 1302 Che H., Xia, X., Zhu, J., Li, Z., Dubovik, O., Holben, B., Goloub, P., Chen, H., Estelles, V.,
1303 Cuevas-Agulló, E., Blarel, L., Wang, H., Zhao, H., Zhang, X., Wang, Y., Sun, J., Tao, R.,
1304 Zhang, X., and Shi, G.: Column aerosol optical properties and aerosol radiative forcing
1305 during a serious haze-fog month over North China Plain in 2013 based on ground-based
1306 sunphotometer measurements, *Atmos. Chem. Phys.*, 14, 2125–2138,
1307 doi:10.5194/acp-14-2125-2014, 2014.
- 1308 Chen, L., Zhu, J., Liao, H., Gao, Y., Qiu, Y., Zhang, M. G., Liu, Z. R., Li, N., and Wang, Y. S.:
1309 Assessing the formation and evolution mechanisms of severe haze pollution in the
1310 Beijing–Tianjin–Hebei region using process analysis, *Atmos. Chem. Phys.*, 19, 10845–
1311 10864, 2019.
- 1312 Cheng, Y., Zheng, G., Wei, C., Mu, Q., Zheng, Bo., Wang, Z., Gao, M., Zhang, Q., He, K.,
1313 Carmichael, G., Pösch, U., and Su, H.: Reactive nitrogen chemistry in aerosol water as a
1314 source of sulfate during haze events in China, *Sci. Adv.*, 2, e1601530, 2016.
- 1315 Dawson, J. P., Adams, P. J., and Pandis, S. N.: Sensitivity of PM_{2.5} to climate in the Eastern
1316 US: a modeling case study, *Atmos. Chem. Phys.*, 7, 4295–4309, 2007.
- 1317 Dickinson, R.E., Henderson-Sellers, A., and Kennedy, P.J.: Biosphere-Atmosphere Transfer
1318 Scheme (BATS) Version 1e as coupled to NCAR Community Climate Model, NCAR
1319 Technical Note, NCAR/TN-387+STR, p.72, 1993.
- 1320 Ding, A., Huang, X., Nie, W., Sun, J., Kerminen, V. M., Petäjä, T., Su, H., Cheng, Y., Yang,
1321 X., Wang, M., Chi, X., Wang, J., Virkkula, A., Guo, W., Yuan, J., Wang, S., Zhang, R.,
1322 Wu, Y., Song, Y., Zhu, T., Zilitinkevich, S., Kulmala, M., and Fu, C.: Enhanced haze
1323 pollution by black carbon in megacities in China, *Geophys. Res. Lett.*, 43, 2873-2879,
1324 10.1002/2016gl067745, 2016.
- 1325 Emmons, L. K., Walters, S., Hess, P. G., Lamarque, J. F., Pfister, G. G., Fillmore, D., Granier,
1326 C., Guenther, A., Kinnison, D., Laepple, T., Orlando, J., Tie, X., Tyndall, G.,
1327 Wiedinmyer, C., Baughcum, S. L., and Kloster, S.: Description and evaluation of the
1328 Model for Ozone and Related chemical Tracers, version 4 (MOZART-4), *Geosci. Model*
1329 *Dev.*, 3, 43-67, doi:10.5194/gmd-3-43-2010, 2010.
- 1330 Forkel, R., Werhahn, J., Hansen, A. B., McKeen, S., Peckham, S., Grell, G., and Suppan, P.:
1331 Effect of aerosol–radiation feedback on regional air quality – a case study with
1332 WRF/Chem, *Atmos. Environ.*, 53, 202–211, 2012.
- 1333 Fountoukis, C. and Nenes, A.: ISORROPIA II: a computationally efficient thermodynamic



- 1334 equilibrium model for $K^+Ca^{2+}Mg^{2+}NH_4^+Na^+SO_4^{2-}NO_3^-Cl^-H_2O$ aerosols,
1335 *Atmos. Chem. Phys.*, 7, 4639-4659, 2007.
- 1336 Fu, C.B., Wang, S.Y., Xiong, Z., Gutowski, W.J., Lee, D., McGregor, J.L., Sato, Y., Kato, H.,
1337 Kim, J., and Suh, M.: Regional climate model intercomparison project for Asia, *Bull.*
1338 *Amer. Meteor. Soc.*, 86, 257-266, 2005.
- 1339 Fu, H. and Chen, J.: Formation, features and controlling strategies of severe haze-fog
1340 pollutions in China, *Sci. Total. Environ.*, 578, 121–138, 2017.
- 1341 Gao, M., Carmichael, G. R., Wang, Y., Saide, P. E., Yu, M., Xin, J., Liu, Z., and Wang, Z.:
1342 Modeling study of the 2010 regional haze event in the North China Plain, *Atmos. Chem.*
1343 *Phys.*, 16, 1673-1691, 10.5194/acp-16-1673-2016, 2016.
- 1344 Gao, M., Han, Z., Liu, Z., Li, M., Xin, J., Tao, Z., Li, J., Kang, J., Huang, K., Dong, X.,
1345 Zhuang, B., Li, S., Ge, B., Wu, Q., Cheng, Y., Wang, Y., Lee, H., Kim, C., Fu, J. S.,
1346 Wang, T., Chin, M., Woo, J., Zhang, Q., Wang, Z., and Carmichael G. R.: Air Quality
1347 and Climate Change, Topic 3 of the Model Inter-Comparison Study for Asia Phase III
1348 (MICS-Asia III), Part I: overview and model evaluation, *Atmos. Chem. Phys.*, 18, 4859–
1349 4884, <https://doi.org/10.5194/acp-18-4859-2018>, 2018.
- 1350 Gao, M., Han, Z. W., Tao, Z. N., Li, J. W., Kang, J.-E., Huang, K., Dong, X. Y., Zhuang, B. L.,
1351 Li, S., Ge, B. Z., Wu, Q. Z., Lee, H.-J., Kim, C. H., Fu, J. S., Wang, T. J., Chin, M., Li,
1352 M., Woo, J.-H., Zhang, Q., Cheng, Y. F., Wang, Z. F., and Carmichael, G. R.: Air quality
1353 and climate change, Topic 3 of the Model Inter-Comparison Study for Asia Phase III
1354 (MICS-Asia III) – Part 2: aerosol radiative effects and aerosol feedbacks. *Atmospheric*
1355 *Chemistry and Physics*, 20, 1147–1161, 2020.
- 1356 Gao, Y., Zhang, M., Liu, Z., Wang, L., Wang, P., Xia, X., Tao, M., and Zhu, L.: Modeling the
1357 feedback between aerosol and meteorological variables in the atmospheric boundary
1358 layer during a severe fog–haze event over the North China Plain, *Atmos. Chem. Phys.*,
1359 15, 4279-4295, 10.5194/acp-15-4279-2015, 2015.
- 1360 Gery, M.W., Whitten, G.Z., Killus, J.P., and Dodge, M.C.: A photochemical kinetics
1361 mechanism for urban and regional scale computer modeling, *J. Geophys. Res.*, 94,
1362 12925-12956, 1989.
- 1363 Ghan, S. and Zaveri R.A.: Parameterization of optical properties for hydrated internally
1364 mixed aerosol, *J. Geophys. Res.*, 112, D10201, doi:10.1029/2006JD007927, 2007.
- 1365 Giglio, L., Randerson, J. T., and van der Werf, G. R.: Analysis of daily, monthly, and annual
1366 burned area using the fourth generation Global Fire Emissions Database (GFED4), *J.*
1367 *Geophys. Res.: Biogeosciences*, doi:10.1002/jgrg.20042, 2013.
- 1368 Grell, G.A.: Prognostic evaluation of assumptions used by cumulus parameterizations, *Mon.*
1369 *Weather. Rev.*, 121, 764-787, 1993.
- 1370 Grell, G. A., Peckham, S. E., Schmitz, R., McKeen, S. A., Frost, G., Skamarock, W. C., and
1371 Eder, B.: Fully coupled “online” chemistry within the WRF model, *Atmos. Environ.*, 39,
1372 6957-6975, 10.1016/j.atmosenv.2005.04.027, 2005.
- 1373 Guo, S., Hu, M., Zamora, M. L., Peng, J., Shang, D., Zheng, J., Du, Z., Wu, Z., Shao, M.,
1374 Zeng, L., Molina, M. J., and Zhang, R. : Elucidating severe urban haze formation in
1375 China, *P. Natl. Acad. Sci. USA.*, 111, 17373–17378,
1376 <https://doi.org/10.1073/pnas.1419604111>, 2014.
- 1377 Han, X., Zhang, M. G., Han, Z. W., Xin, J. Y., and Liu, X. H.: Simulation of aerosol direct



- 1378 radiative forcing with RAMS-CMAQ in East Asia, *Atmos. Environ.*, 45, 6576-6592,
1379 2011a.
- 1380 Han, Z. W., Ueda, H., Matsuda, K., Zhang, R. J., Arao, K., Kanai, Y., and Hasome, H.: Model
1381 study on particle size segregation and deposition during Asian dust events in March
1382 2002, *J. Geophys. Res.*, 109, D19205, doi: 10.1029/2004jd004920, 2004.
- 1383 Han, Z. W.: Direct radiative effect of aerosols over East Asia with a Regional coupled
1384 Climate/Chemistry model, *Meteorol. Z.*, Vol. 19, No. 3, 287-298, 2010.
- 1385 Han, Z. W., Xiong, Z., and Li, J. W.: Direct climatic effect of aerosols and interdecadal
1386 variations over East Asia investigated by a regional climate/chemistry model,
1387 *Atmospheric and Oceanic Science Letters*, 4(6), 299-303, 2011b.
- 1388 Han, Z. W., Li, J. W., Xia, X. A., and Zhang, R. J.: Investigation of direct radiative effects of
1389 aerosols in dust storm season over East Asia with an online coupled regional
1390 climate-chemistry-aerosol model, *Atmos. Environ.*, 54, 688-699, 2012.
- 1391 Han, Z. W., Li, J. W., Guo, W. D., Xiong, Z., and Zhang, W.: A study of dust radiative
1392 feedback on dust cycle and meteorology over East Asia by a coupled regional
1393 climate-chemistry-aerosol model, *Atmos. Environ.*, 68, 54-63, 2013.
- 1394 Han, Z. W., Li, J. W., Yao, X. H., and Tan, S. C.: A regional model study of the characteristics
1395 and indirect effects of marine primary organic aerosol in springtime over East Asia,
1396 *Atmos. Environ.*, 197, 22–35, 2019.
- 1397 Hess, M., Koepke, P., and Schuit, I.: Optical properties of aerosols and clouds: the software
1398 package OPAC, *Bull. Amer. Meteor. Soc.*, 79, 831-844, 1998.
- 1399 Heo, B.-H., Jacoby-Koaly, S., Kim, K.-E., Campistron, B., Benech, B., and Jung, E.-S.: Use
1400 of the Doppler Spectral Width to Improve the Estimation of the Convective Boundary
1401 Layer Height from UHF Wind Profiler Observations, *J. Atmos. Ocean. Technol.*, 20,
1402 408-424, 2003.
- 1403 Hong, S. and Pan, H.: Nonlocal boundary layer vertical diffusion in a medium-range forecast
1404 model, *Mon. Weather Rev.*, 124, 2322–2339, 1996.
- 1405 Huang, R. J., Zhang, Y., Bozzetti, C., Ho, K. F., Cao, J. J., Han, Y., Daellenbach, K. R.,
1406 Slowik, J. G., Platt, S. M., Canonaco, F., Zotter, P., Wolf, R., Pieber, S. M., Bruns, E. A.,
1407 Crippa, M., Ciarelli, G., Piazzalunga, A., Schwikowski, M., Abbazade, G.,
1408 Schnelle-Kreis, J., Zimmermann, R., An, Z., Szidat, S., Baltensperger, U., El Haddad, I.,
1409 and Prevot, A. S.: High secondary aerosol contribution to particulate pollution during
1410 haze events in China, *Nature*, 514, 218-222, 10.1038/nature13774, 2014.
- 1411 Isaksen I.S.A., Granier, C., Myhre, G., Berntsen, T.K., Dalsøren, S.B., Gauss, M., Klimont, Z.,
1412 Benestad, R., Bousquet, P., Collins, W., Cox, T., Eyring, V., Fowler, D., Fuzzi, S.,
1413 Jočkel, P., Laj, P., Lohmann, U., Maione, M., Monks, P., Prevot, A.S.H., Raes, F.,
1414 Richter, A., Rognerud, B., Schulz, M., Shindell, D., Stevenson, D.S., Storelvmo, T.,
1415 Wang, W.-C., van Weele, M., Wild, M., and Wuebbles, D.: Atmospheric composition
1416 change: Climate–Chemistry interactions, *Atmos. Environ.*, 43, 5138–5192, 2009.
- 1417 Jing, J., Wu, Y., Tao, J., Che, H.Z, Xia, X., Zhang, X., Yan, P., Zhao, D.M., and Zhang, L.M.:
1418 Observation and analysis of near-surface atmospheric aerosol optical properties in urban
1419 Beijing, *Particuology*, 18, 144-154, 2015.
- 1420 Kajino, M., Ueda, H., Han, Z. W., Kudo, R., Inomata, Y., Kaku, H.: Synergy between air
1421 pollution and urban meteorological changes through aerosol-radiation-diffusion



- 1422 feedback—A case study of Beijing in January 2013, *Atmos. Environ.*, 171, 98-110,
1423 2017.
- 1424 Keihl, J.T., Hack, J.J., Bonan, G.B., Boville, B.A., Briegleb, B.P., Williamson, D.L., and
1425 Rasch, P.J.: Description of the NCAR Community Climate Model (CCM3), NCAR
1426 Technical Note, NCAR/TN-420+STR, p.152, 1996.
- 1427 Li, G.H., Bei, N.F., Cao, J.J., Huang, R.J., Wu, J.R., Feng, T., Wang, Y.C., Liu, S.X., Zhang,
1428 Q., Tie, X.X., and Molina, L.T.: A possible pathway for rapid growth of sulfate during
1429 haze days in China, *Atmos. Chem. Phys.*, 17, 3301-3316, 2017c.
- 1430 Li, J., Chen, X.S., Wang, Z.F., Du, H.Y., Yang, W.Y., Sun, Y.L., Hu, B., Li, J.J., Wang, W.,
1431 Wang, T., Fu, P.Q., and Huang, H.L.: Radiative and heterogeneous chemical effects of
1432 aerosols on ozone and inorganic aerosols over East Asia, *Sci. Total. Environ.*, 622-623,
1433 1327-1342, 2018b.
- 1434 Li, J. W. and Han, Z. W.: A modeling study of the impact of heterogeneous reactions on
1435 mineral aerosol surfaces on tropospheric chemistry over East Asia, *Particuology*, 8,
1436 433-441, 2010.
- 1437 Li, J. W., Han, Z. W., and Zhang, R. J.: Influence of aerosol hygroscopic growth
1438 parameterization on aerosol optical depth and direct radiative forcing over East Asia,
1439 *Atmos. Res.*, 140-141, 14-27, 2014.
- 1440 Li, J. W. and Han, Z. W.: A modeling study of severe winter haze events in Beijing and its
1441 neighboring regions, *Atmos. Res.*, 170, 87-97, 2016a.
- 1442 Li, J. W. and Han, Z. W.: Aerosol vertical distribution over east China from RIEMS-Chem
1443 simulation in comparison with CALIPSO measurements, *Atmos. Environ.*, 143, 177-189,
1444 2016b.
- 1445 Li, J. W. and Han, Z. W.: Seasonal variation of nitrate concentration and its direct radiative
1446 forcing over East Asia, *Atmosphere*, 7(8), 105, 2016c.
- 1447 Li, J. W., Han, Z. W., and Yao, X. H.: A modeling study of the influence of sea salt on
1448 inorganic aerosol concentration, size distribution, and deposition in the western Pacific
1449 Ocean, *Atmos. Environ.*, 188, 157-173, 2018a.
- 1450 Li, J. W., Han, Z. W., Yao, X. H., Xie, Z. X., and Tan, S. C.: The distributions and direct
1451 radiative effects of marine aerosols over East Asia in springtime, *Sci. Total. Environ.*,
1452 651, 1913-1925, 2019b.
- 1453 Li, M., Zhang, Q., Kurokawa, J.-I., Woo, J.-H., He, K., Lu, Z., Ohara, T., Song, Y., Streets, D.
1454 G., Carmichael, G. R., Cheng, Y., Hong, C., Huo, H., Jiang, X., Kang, S., Liu, F., Su, H.,
1455 and Zheng, B.: MIX: a mosaic Asian anthropogenic emission inventory under the
1456 international collaboration framework of the MICS-Asia and HTAP, *Atmos. Chem.
1457 Phys.*, 17, 935-963, 10.5194/acp-17-935-2017, 2017a.
- 1458 Li X., Wu, J., Elser, M., Tong, S., Liu, S., Li, X., Liu, L., Cao, J., Zhou, J., El-Haddad, I.,
1459 Huang, R., Ge, M., Tie, X., André S. H. Prévôt, and Li, G.: Wintertime secondary
1460 organic aerosol formation in Beijing-Tianjin-Hebei (BTH): contributions of HONO
1461 sources and heterogeneous reactions, *Atmos. Chem. Phys.*, 19, 2343-2359,
1462 <https://doi.org/10.5194/acp-19-2343-2019>, 2019a.
- 1463 Li, Z., Guo, J., Ding, A., Liao, H., Liu, J., Sun, Y., Wang, T., Xue, H., Zhang, H., and Zhu, B.:
1464 Aerosol and boundary-layer interactions and impact on air quality, *Natl. Sci. Rev.*, 4,
1465 810-833, 10.1093/nsr/nwx117, 2017b.



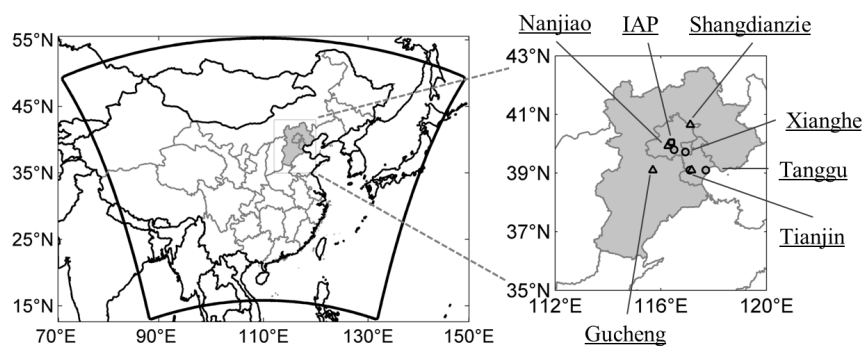
- 1466 Liu, X. H. and Wang, J.: How important is organic aerosol hygroscopicity to aerosol indirect
1467 forcing? *Environ. Res. Lett.*, 5(4), 044010,
1468 <http://iopscience.iop.org/1748-9326/5/4/044010>, 2010a.
- 1469 Liu, X. H., Zhang, Y., Xing, J., Zhang, Q., Wang, K., Streets, D., Jang, C., Wang, W.-X., and
1470 Hao, J.-M.: Understanding of regional air pollution over China using CMAQ, part II.
1471 Process analysis and sensitivity of ozone and particulate matter to precursor emissions,
1472 *Atmos. Environ.*, 44, 3719–3727, 2010b.
- 1473 Ma, N., Zhao, C. S., Müller, T., Cheng, Y. F., Liu, P. F., Deng, Z. Z., Xu, W. Y., Ran, L., Nekat,
1474 B., van Pinxteren, D., Gnauk, T., Müller, K., Herrmann, H., Yan, P., Zhou, X.J., and
1475 Wiedensohler, A.: A new method to determine the mixing state of light absorbing
1476 carbonaceous using the measured aerosol optical properties and number size
1477 distributions, *Atmos. Chem. Phys.*, 12, 2381–2397, 2012.
- 1478 Ma, Q. X., Wu, Y. F., Zhang, D. Z., Wang, X. J., Xia, Y. J., Liu, X. Y., Tian, P., Han, Z. W.,
1479 Xia, X. A., Wang, Y., and Zhang, R. J.: Roles of regional transport and heterogeneous
1480 reactions in the PM_{2.5} increase during winter haze episodes in Beijing, *Sci. Total*
1481 *Environ.*, 599–600, 246–253, 2017.
- 1482 NOAA/NCEP.: NCEP FNL Operational Model Global Tropospheric Analyses, continuing
1483 from July 1999. Research Data Archive at the National Center for Atmospheric Research,
1484 Computational and Information Systems Laboratory, Dataset.
1485 <https://doi.org/10.5065/D6M043C6>, Last accessed, 12 April 2019, 2000.
- 1486 Odum, J.R., Jungkamp, T.P.W., Griffin, R.J., Flagan, R.C., and Seinfeld, J.H.: The
1487 atmospheric aerosol-forming potential of whole gasoline vapor, *Science*. 276, 96–99,
1488 1997.
- 1489 Petters, M.D. and Kreidenweis, S.M.: A single parameter representation of hygroscopic
1490 growth and cloud condensation nucleus activity, *Atmos. Chem. Phys.*, 7, 1961–1971,
1491 2007.
- 1492 Qiu, Y., Liao, H., Zhang, R., and Hu, J.: Simulated impacts of direct radiative effects of
1493 scattering and absorbing aerosols on surface layer aerosol concentrations in China
1494 during a heavily polluted event in February 2014, *J. Geophys. Res.:Atmospheres*, 122,
1495 5955–5975, 10.1002/2016jd026309, 2017.
- 1496 Ramanathan, V., Crutzen, P. J., Kiehl, J. T., and Rosenfeld, D.: Aerosols, climate, and the
1497 hydrological cycle, *Science*, 294, 2119–2124, 10.1126/science.1064034, 2001.
- 1498 Riemer, N., West, M., Zaveri, R., and Easter, R.: Estimating black carbon aging time-scales
1499 with a particle-resolved aerosol model, *J. Aerosol Sci.*, 41, 143–158, 2010.
- 1500 Song, Z.J., Fu, D.S., Zhang, X.L., Wu, Y.F., Xia, X.A., He, J.X., Han, X.L., Zhang, R.J., and
1501 Che, H.Z.: Diurnal and seasonal variability of PM_{2.5} and AOD in North China plain:
1502 Comparison of MERRA-2 products and ground measurements, *Atmos. Environ.*, 191,
1503 70–78, 2018.
- 1504 Sun, Y., Jiang, Q., Wang, Z., Fu, P., Li, J., Yang, T., and Yin, Y.: Investigation of the Sources
1505 and Evolution Processes of Severe Haze Pollution in Beijing in January 2013, *J.*
1506 *Geophys. Res.*, 119, 4380–4398, 2014.
- 1507 Twomey, S.: Pollution and the planetary albedo, *Atmos. Environ.*, 8, 1251–1256, 1974.
- 1508 Wang, J., Wang, S., Jiang, J., Ding, A., Zheng, M., Zhao, B., Wong, D. C., Zhou, W., Zheng,
1509 G., and Wang, L.: Impact of aerosol-meteorology interactions on fine particle pollution



- 1510 during China's severe haze episode in January 2013, *Environ. Res. Lett.*, 9, 094002,
1511 <https://doi.org/10.1088/1748-9326/9/9/094002>, 2014b.
- 1512 Wang, S. Y., Fu, C. B., Wei, H. L., Qian, Y., Xiong, Z., Feng, J.M., Zhao, D. M., Dan, L., Han,
1513 Z.W., Su, B.K., Zhao, M., Zhang, Y.C., Tang, J.P., Liu, H.N., Wu, J., Zeng, X.M., Chen,
1514 M., and Wang, L.Z.: Regional integrated environmental modeling system: development
1515 and application, *Climate Change*, 129, 499-510, 2015.
- 1516 Wang, Y., Bao, S., Wang, S., Hu, Y., Shi, X., Wang, J., Zhao, B., Jiang, J., Zheng, M., Wu, M.,
1517 Russell, A. G., Wang, Y., and Hao, J.: Local and regional contributions to fine particulate
1518 matter in Beijing during heavy haze episodes, *Sci. Total. Environ.*, 580, 283-296,
1519 [10.1016/j.scitotenv.2016.12.127](https://doi.org/10.1016/j.scitotenv.2016.12.127), 2017.
- 1520 Wang, Z., Li, J., Wang, Z., Yang, W., Tang, X., Ge, B., Yan, P., Zhu, L., Chen, X., Chen, H.,
1521 Wand, W., Li, J., Liu, B., Wang, X., Wand, W., Zhao, Y., Lu, N., and Su, D.: Modeling
1522 study of regional severe hazes over mid-eastern China in January 2013 and its
1523 implications on pollution prevention and control, *Sci. China. Earth. Sci.*, 57, 3-13,
1524 [10.1007/s11430-013-4793-0](https://doi.org/10.1007/s11430-013-4793-0), 2014a.
- 1525 Westervelt, D. M., Moore, R. H., Nenes, A. and Adams, P.J.: Effect of primary organic sea
1526 spray emissions on cloud condensation nuclei concentrations, *Atmos. Chem. Phys.*, 12,
1527 89–101, 2012.
- 1528 Wu J., Bei, N., Hu, B., Liu, S., Zhou, M., Wang, Q., Li, X., Liu, L., Feng, T., Liu, Z., Wang,
1529 Y., Cao, J., Tie, X., Wang J., Molina, L.T., and Li, G.: Aerosol–radiation feedback
1530 deteriorates the wintertime haze in the North China Plain, *Atmos. Chem. Phys.*, 19,
1531 8703–8719, <https://doi.org/10.5194/acp-19-8703-2019>, 2019.
- 1532 Wu, Y. F., Zhang, R. J., Tian, P., Tao, J., Hsu, S.-C., Yan, P., Wang, Q. Y., Cao, J. J., Zhang, X.
1533 L., and Xia, X. A.: Effect of ambient humidity on the light absorption amplification of
1534 black carbon in Beijing during January 2013, *Atmos. Environ.*, 124, 217-223 , 2016.
- 1535 Xiong, Z., Fu, C. B., and Yan, X. D.: Regional Integrated environmental model system and its
1536 simulation of East Asia summer monsoon, *Chinese. Sci. Bull.*, 54(22), 4253-4261, 2009.
- 1537 Yu S., Mathur, R., Schere, K., Kang, D., Plein, J., Young, J., Tong, D., Pouliot, G., Mckeen,
1538 S.A., and Rao, S. T.: Evaluation of real-time PM_{2.5} forecasts and process analysis for
1539 PM_{2.5} formation over the eastern United States using the Eta-CMAQ forecast model
1540 during the 2004 ICARTT study, *J. Geophys. Res.*, 113, D06204, doi:
1541 [10.1029/2007JD009226](https://doi.org/10.1029/2007JD009226), 2008.
- 1542 Zhang, B., Wang, Y., and Hao, J.: Simulating aerosol–radiation–cloud feedbacks on
1543 meteorology and air quality over eastern China under severe haze conditions in winter,
1544 *Atmos. Chem. Phys.*, 15, 2387-2404, [10.5194/acp-15-2387-2015](https://doi.org/10.5194/acp-15-2387-2015), 2015.
- 1545 Zhang, X. Y., Wang, Y. Q., Niu, T., Zhang, X. C., Gong, S. L., Zhang, Y. M., and Sun, J. Y.:
1546 Atmospheric aerosol compositions in China: spatial/temporal variability, chemical
1547 signature, regional haze distribution and comparisons with global aerosols, *Atmos.*
1548 *Chem. Phys.*, 12, 779–799, <https://doi.org/10.5194/acp-12-779-2012>, 2012.
- 1549 Zhang, X., Zhong, J., Wang, J., Wang, Y., and Liu, Y.: The interdecadal worsening of weather
1550 conditions affecting aerosol pollution in the Beijing area in relation to climate warming,
1551 *Atmos. Chem. Phys.*, 18, 5991–5999, <https://doi.org/10.5194/acp-18-5991-2018>, 2018a.
- 1552 Zhang X., Zhang, Q., Hong, C., Zheng, Y., Geng, G., Tong, D., Zhang, Y. and Zhang, X.:
1553 Enhancement of PM_{2.5} Concentrations by Aerosol-Meteorology Interactions Over China,

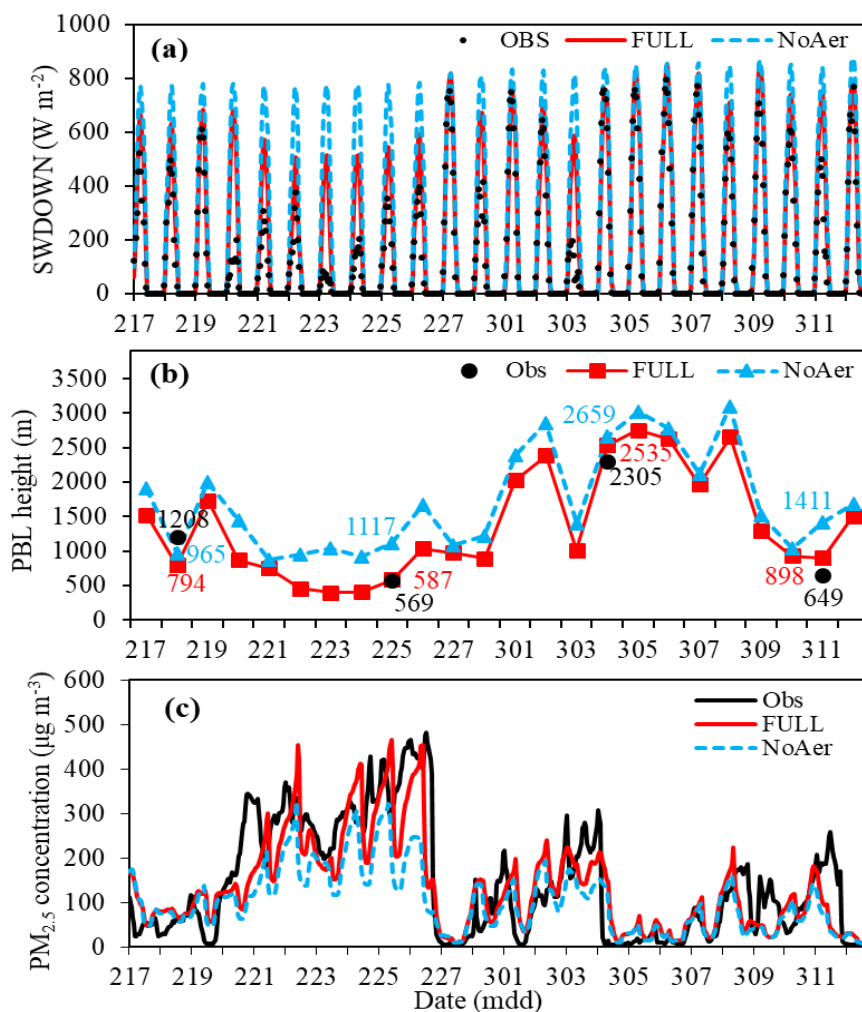


- 1554 J. Geophys. Res.: Atmospheres, 123, <https://doi.org/10.1002/2017JD027524>, 2018b.
- 1555 Zhang, Y.: Online coupled meteorology and chemistry models: history, current status, and
1556 outlook, *Atmos. Chem. Phys.*, 8, 2895-2932, 2008.
- 1557 Zhang, Y., Wen, X.-Y., Wang, K., Vijayaraghavan, K., and Jacobson, M. Z.: Probing into
1558 regional O₃ and PM pollution in the U.S., Part II. An examination of formation
1559 mechanisms through a process analysis technique and sensitivity study, *J. Geophys.*
1560 *Res.*, 114 (D22305), doi:10.1029/2009JD011900, 2009.
- 1561 Zhang, Y., Wen, X. Y., and Jang, C. J.: Simulating chemistry-aerosol-cloud-radiation-climate
1562 feedbacks over the continental U.S. using the online-coupled weather research
1563 forecasting model with chemistry (WRF/Chem), *Atmos. Environ.*, 44, 3568–3582, 2010.
- 1564 Zhao, B., Liou, K. N., Gu, Y., Li, Q., Jiang, J. H., Su, H., He, C., Tseng, H. R., Wang, S., Liu,
1565 R., Qi, L., Lee, W. L., and Hao, J.: Enhanced PM_{2.5} pollution in China due to
1566 aerosol-cloud interactions, *Sci. Rep.*, 7, 4453, [10.1038/s41598-017-04096-8](https://doi.org/10.1038/s41598-017-04096-8), 2017.
- 1567 Zhao, D.M.: Performance of Regional Integrated Environment Modeling System (RIEMS) in
1568 precipitation simulations over East Asia, *Clim. Dynam.* 40, 1767-1787, 2013.
- 1569 Zhao, P., Dong, F., Yang, Y., He, D., Zhao, X., and Zhang, W.: Characteristics of
1570 carbonaceous aerosol in the region of Beijing, Tianjin, and Hebei, China, *Atmos.*
1571 *Environ.*, 71, 389–398, 2013.
- 1572 Zheng, B., Zhang, Q., Zhang, Y., He, K. B., Wang, K., Zheng, G. J., Duan, F. K., Ma, Y. L.,
1573 and Kimoto, T.: Heterogeneous chemistry: a mechanism missing in current models to
1574 explain secondary inorganic aerosol formation during the January 2013 haze episode in
1575 North China, *Atmos. Chem. Phys.*, 15, 2031–2049, doi:10.5194/acp-15-2031-2015,
1576 2015.
- 1577 Zhong, J., Zhang, X., Dong, Y., Wang, Y., Liu, C., Wang, J., Zhang, Y., and Che, H.: Feedback
1578 effects of boundary-layer meteorological factors on cumulative explosive growth of
1579 PM_{2.5} during winter heavy pollution episodes in Beijing from 2013 to 2016, *Atmos.*
1580 *Chem. Phys.*, 18, 247–258, <https://doi.org/10.5194/acp-18-247-2018>, 2018a.
- 1581 Zhong, J., Zhang, X., Wang, Y., Liu, C., and Dong, Y.: Heavy aerosol pollution episodes in
1582 winter Beijing enhanced by radiative cooling effects of aerosols, *Atmos. Res.*, 209, 59–
1583 64, <https://doi.org/10.1016/j.atmosres.2018.03.011>, 2018b.
- 1584 Zhuang, B. L., Li, S., Wang, T. J., Deng, J. J., Xie, M., Yin, C. Q., and Zhu, J. L.: Direct
1585 radiative forcing and climate effects of anthropogenic aerosols with different mixing
1586 states over China, *Atmos. Environ.*, 79, 349-361, 2013.
- 1587
- 1588
- 1589
- 1590
- 1591
- 1592
- 1593
- 1594



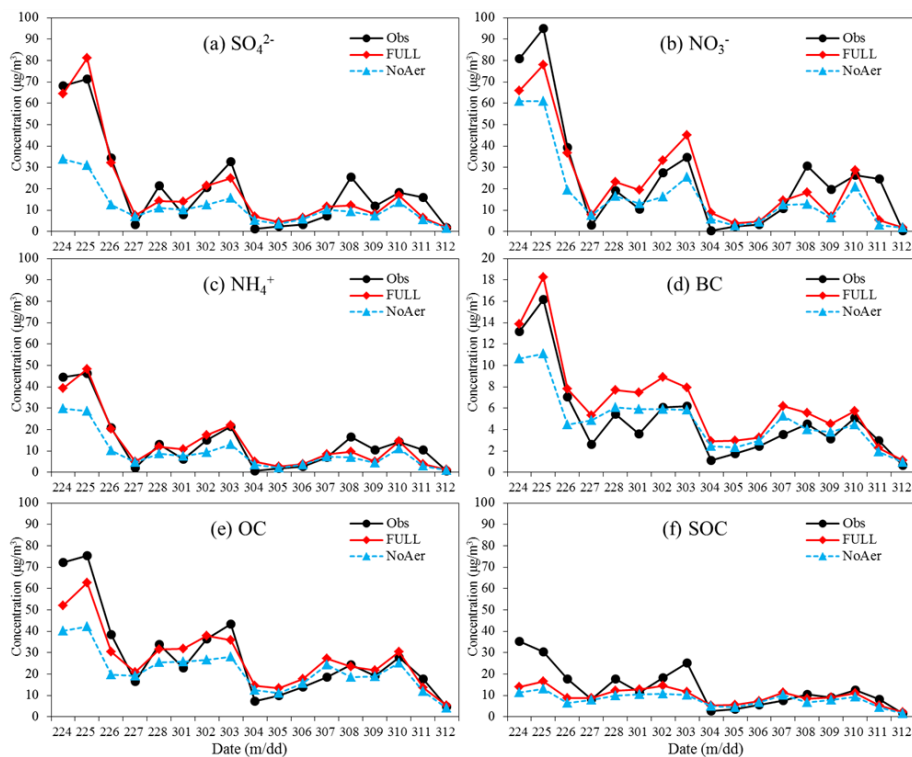
1595

1596 Figure 1. The model study domain. The shaded areas indicate the Beijing-Tianjin-Hebei
1597 (BTH) region. Markers are observation sites (square: IAP, observations of PM_{2.5}, its chemical
1598 components, aerosol extinction coefficient (EXT) and aerosol absorption coefficient (ABS);
1599 circles: observations of meteorological variables; triangles: aerosol optical depth. The
1600 Xianghe site provides meteorological soundings and hourly surface shortwave radiation
1601 (SWDOWN) measurements, the Tianjin site provides both meteorological variables and
1602 AOD).



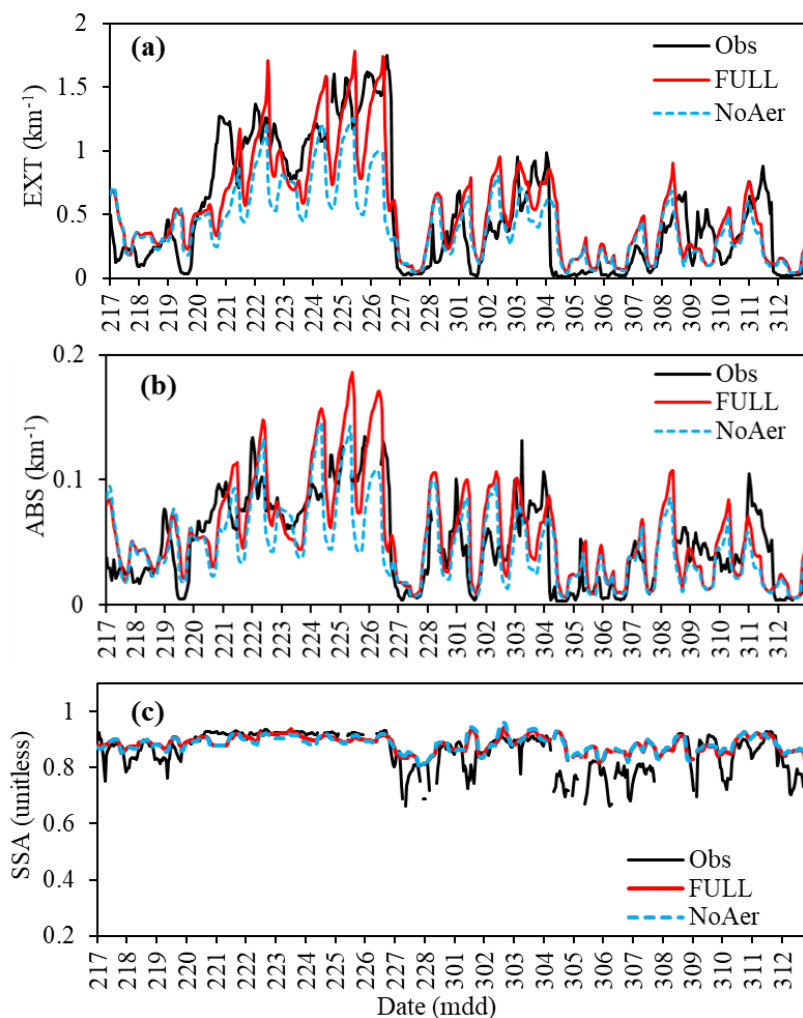
1603

1604 Figure 2. The model simulated and observed (a) hourly SWDOWN at Xianghe, (b) hourly
1605 PBL height at 14:00 (LST) at Xianghe (note observations are available in the 4 days, numbers
1606 are observations and corresponding simulations) and (c) hourly $\text{PM}_{2.5}$ concentration at IAP in
1607 Beijing.



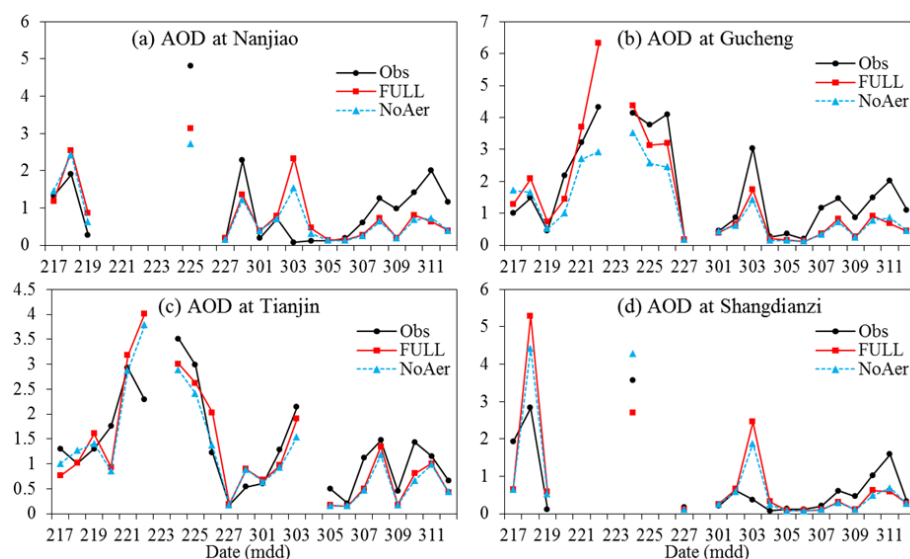
1608

1609 Figure 3. The model simulated and observed daily mean concentrations of aerosol
1610 compositions in PM_{2.5} at the IAP site in Beijing.



1611

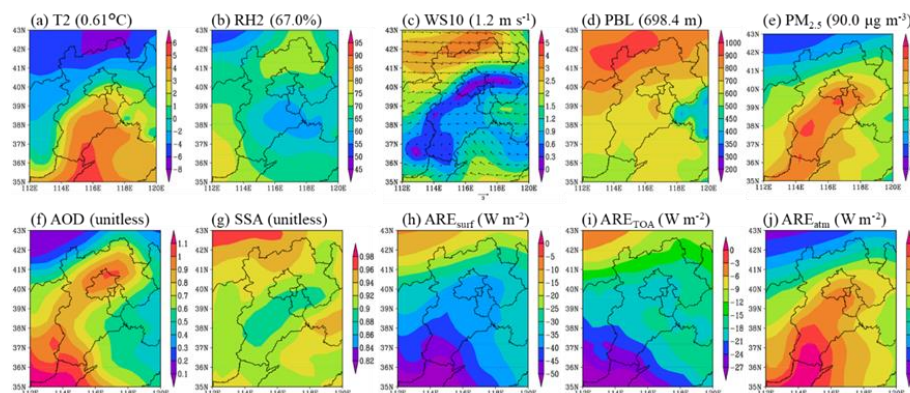
1612 Figure 4. The model simulated and observed hourly (a) aerosol extinction coefficient (EXT),
1613 (b) absorption coefficient (ABS) and (c) single scattering albedo (SSA) at the IAP site in
1614 Beijing under dry condition (RH=10%).



1615

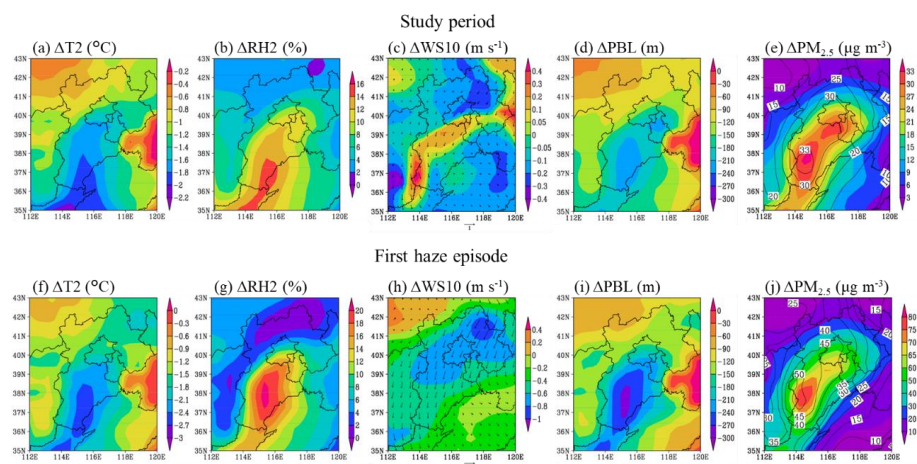
1616 Figure 5. The model simulated and observed daily mean AOD (at 550 nm) at the four sites of
 1617 CARSNET.

1618



1619

1620 Figure 6. The model simulated (a) air temperature (T2), (b) relative humidity (RH2), (c) wind
 1621 speed (WS10), (d) PBL height, (e) PM_{2.5} concentration, (f) AOD, (g) SSA, (h) all-sky ARE at
 1622 the surface, (i) all-sky ARE at the top of atmosphere and (j) all-sky ARE in the atmosphere
 1623 from the FULL case. Numbers in the parentheses are averages over the BTH region during
 1624 the entire study period.



1625

1626 Figure 7. The model simulated feedback-induced changes (FULL minus NoAer) in (a, f) air
1627 temperature (T2), (b, g) relative humidity (RH2), (c, h) wind speed (WS10), (d, i) PBL height
1628 and (e, j) PM_{2.5} concentration averaged over the entire study period (a-e) and over the first
1629 haze episode (20-26 February) (f-j). Units are given in the parentheses.

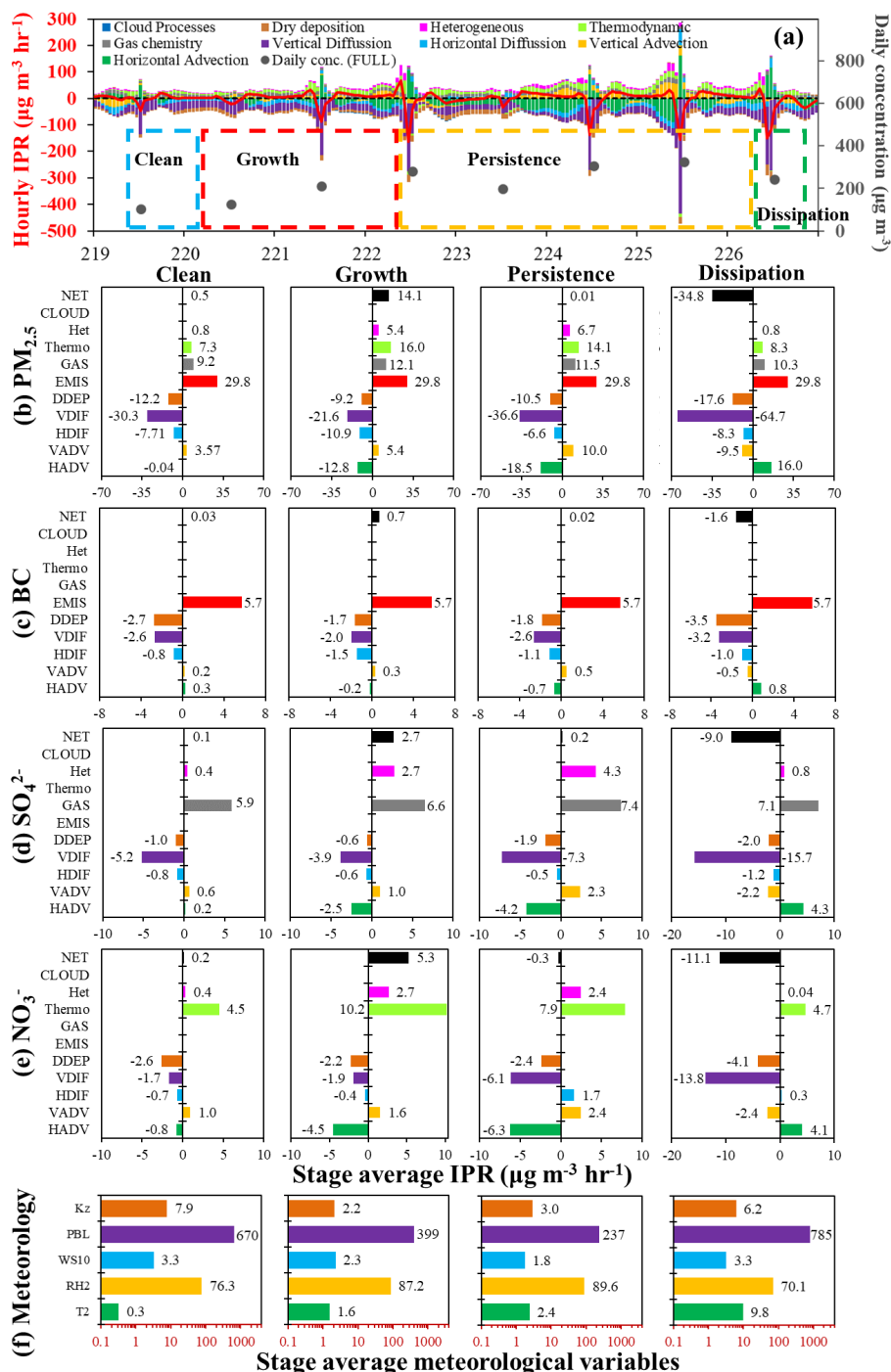


Figure 8. The model calculated integrated process rates (IPR) for the first haze episode (20-26 February) in Beijing. (a) hourly IPR, daily PM_{2.5} concentration and the division of the four stages. The constant IPRs of emissions are not shown for clarity. The mean IPRs for (b) PM_{2.5}, (c) BC, (d) sulfate (SO₄²⁻), nitrate (NO₃⁻), and (f) mean meteorological variables in the four stages. Note that zero IPR



values are not listed. Units of T2, RH2, WS10, PBL and K_z are °C, %, m s^{-1} , m and $\text{m}^2 \text{s}^{-1}$, respectively.

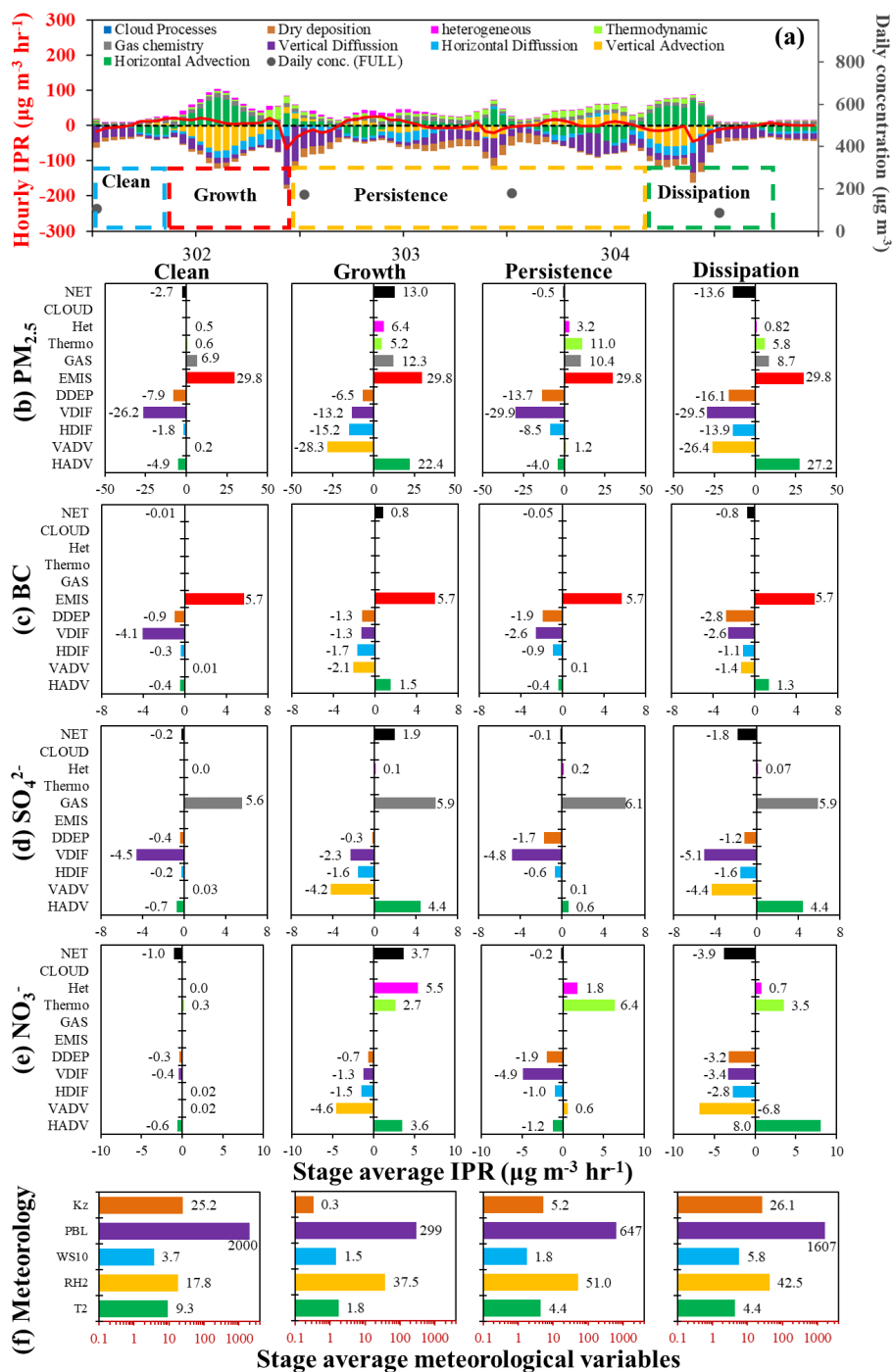


Figure 9. Same as Figure 8 but for the second haze episode (1-4 March).

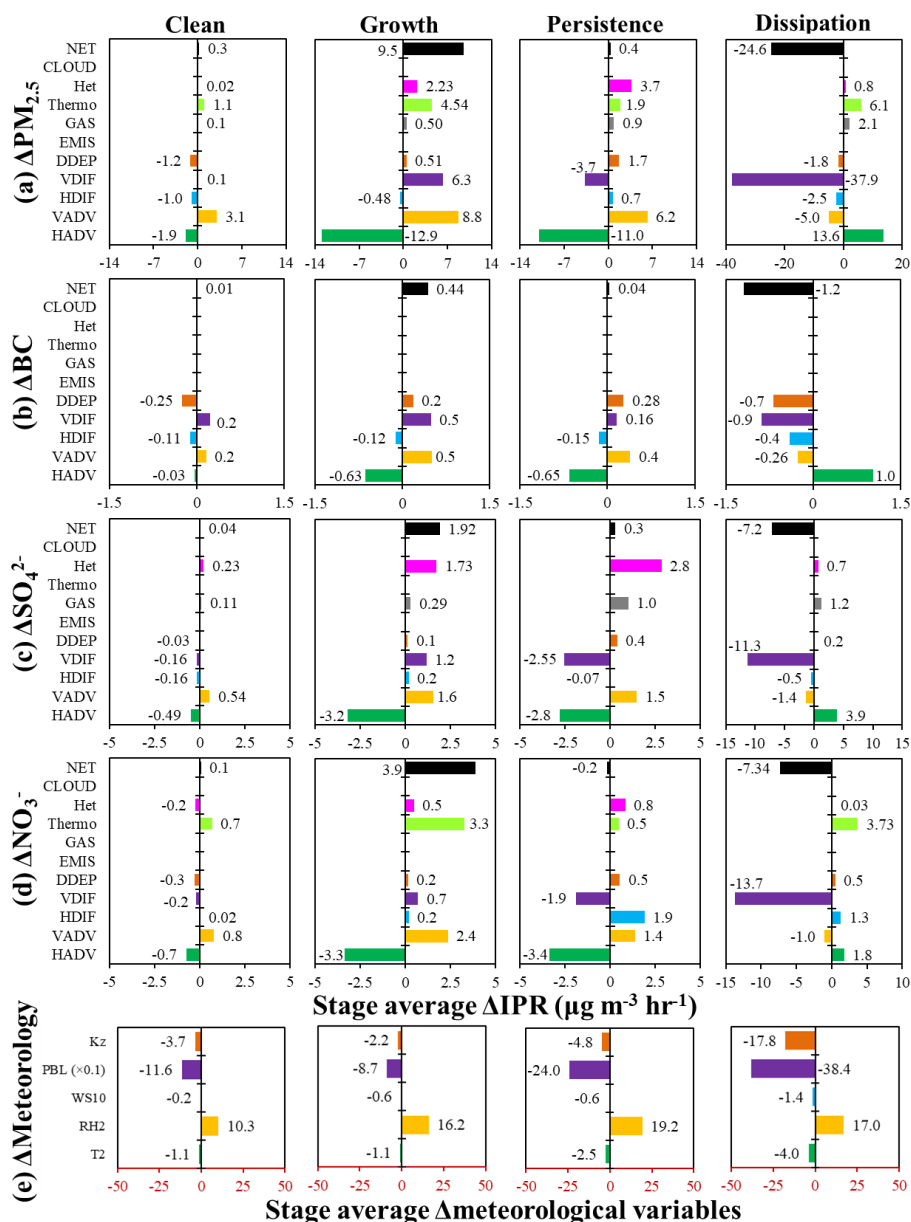


Figure 10. The feedback-induced mean changes in IPRs (FULL minus NoAer) for $PM_{2.5}$ and its chemical components and meteorological variables during the first haze episode (20–26 February) in Beijing. ΔIPR s for $PM_{2.5}$ and its chemical components and Δ meteorological variables are averages over the four stages. Note that zero ΔIPR values (no change) are not shown and the ΔPBL heights are scaled by 0.1. The division of the four stages and units are the same as those in Figure 8.

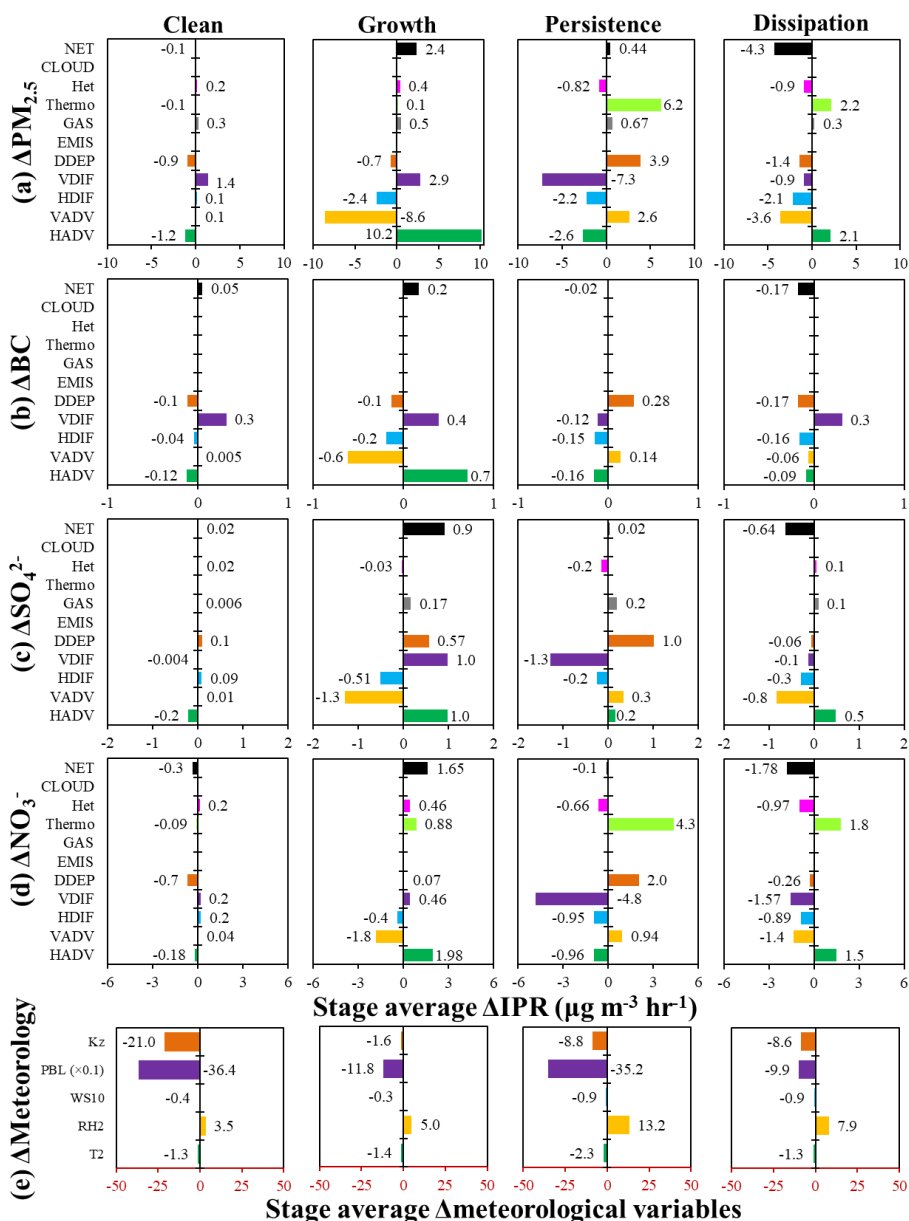


Figure 11. Same as Figure 10 but for the second haze episode (1-4 March). The division of the four stages are the same as that in Figure 9.



Table 1. Performance statistics for meteorological variables at observation sites in the BTH region. Mean observation (Obs), mean simulation (Sim), correlation coefficient (R) and normalized mean bias (NMB in %) are given. WS10, T2 and RH2 are wind speed at 10 meter, air temperature at 2 meter and relative humidity at 2 meter, respectively. All the sample numbers are 207.

Sites	Longitude	Latitude	WS10 (m s^{-1})				T2 ($^{\circ}\text{C}$)				RH2 (%)				SWDOWN (W m^{-2})			
			Obs	Sim	R	NMB	Obs	Sim	R	NMB	Obs	Sim	R	NMB	Obs	Sim	R	NMB
FULL																		
Beijing	39°48'N	116°30'E	2.3	2.9	0.53	28%	3.0	2.5	0.77	-16%	53.4	62.6	0.72	17%				
Tianjin	39°6'N	117°6'E	2.6	3.1	0.53	23%	3.5	3.8	0.89	8%	62.9	59.2	0.68	-6%				
Tangu	39°6'N	117°42'E	2.4	3.4	0.36	42%	3.0	3.1	0.84	2%	69.3	61.3	0.49	-12%				
Total			2.4	3.1	0.47	31%	3.2	3.1	0.83	-2%	61.9	61.0	0.61	-1%				
Xianghe	39°45'N	116°58'E													136.0	188.4	0.91	38%
NoAer																		
Beijing	39°48'N	116°30'E	2.3	3.4	0.48	48%	3.0	4.1	0.74	37%	53.4	51.1	0.68	-4%				
Tianjin	39°6'N	117°6'E	2.6	3.6	0.48	39%	3.5	5.3	0.88	51%	62.9	47.8	0.65	-24%				
Tangu	39°6'N	117°42'E	2.4	3.8	0.28	60%	3.0	4.5	0.84	50%	69.3	51.4	0.48	-26%				
Total			2.4	3.6	0.41	49%	3.2	4.6	0.82	46%	61.9	50.1	0.59	-19%				
Xianghe	39°45'N	116°58'E													136.0	234.0	0.85	72%



Table 2. Performance statistics for PM_{2.5} concentration and its chemical components, aerosol optical parameters at RH=10% (EXT, ABS and SSA) at the IAP site in Beijing. Mean observation (Obs), mean simulation (Sim), correlation coefficient (R) and normalized mean bias (NMB in %) are listed.

Species (unit)	Samples	Obs	FULL			NoAer		
			Sim	R	NMB	Sim	R	NMB
PM _{2.5} (μg m ⁻³)	570	142.0	131.4	0.80	-7%	101.2	0.73	-29%
SO ₄ ²⁻ (μg m ⁻³)	33	21.0	20.3	0.92	-4%	11.9	0.88	-44%
NO ₃ ⁻ (μg m ⁻³)	33	26.0	24.3	0.88	-6%	17.6	0.87	-32%
NH ₄ ⁺ (μg m ⁻³)	33	14.1	13.9	0.91	-2%	9.4	0.89	-34%
BC (μg m ⁻³)	33	5.2	6.7	0.92	28%	5.0	0.84	-3%
OC (μg m ⁻³)	33	29.1	28.3	0.88	-3%	22.3	0.78	-24%
POC (μg m ⁻³)	33	15.5	18.4	0.93	19%	14.1	0.87	-9%
SOC (μg m ⁻³)	33	13.6	9.9	0.56	-27%	8.2	0.45	-40%
EXT (km ⁻¹)	570	0.51	0.53	0.79	4%	0.41	0.72	-19%
ABS (km ⁻¹)	534	0.048	0.052	0.68	10%	0.043	0.59	-11%
SSA (unitless)	534	0.85	0.88	0.65	5%	0.88	0.59	5%



Table 3. Performance statistics for daily mean AOD at the four CARSNET sites in the BTH region. Mean observation (Obs), mean simulation (Sim), correlation coefficient (R) and normalized mean bias (NMB, in the unit of %) are listed.

	Samples	Obs	FULL			NoAer		
			Sim	R	NMB	Sim	R	NMB
Nanjiao	18	1.09	0.92	0.67	-15.6%	0.82	0.74	-24.9%
Gucheng	22	1.73	1.51	0.90	-12.8%	1.16	0.91	-33.0%
Tianjin	22	1.37	1.29	0.86	-5.7%	1.19	0.86	-12.8%
Shangdianzi	17	0.84	0.90	0.72	6.2%	0.89	0.85	5.0%
Total	79	1.29	1.18	0.81	-8.6%	1.03	0.82	-20.2%

Table 4. The model simulated domain and period averages of AOD, SSA and AREs from the FULL case over the BTH region.

	AOD (unitless)	SSA (unitless)	ARE _{surf} (W m ⁻²)	ARE _{TOA} (W m ⁻²)	ARE _{atm} (W m ⁻²)
Study period (Feb 17 - Mar 12)					
All day	0.78	0.91	-37	-18	19
Daytime	1.53	0.92	-79	-39	40
Haze episode 1 (Feb 20-26)					
All day	1.59	0.93	-57	-32	25
Daytime	3.17	0.93	-123	-69	53



Table 5. The model simulated feedback-induced changes (FULL minus NoAer) in T2, WS10, RH2, PBL height, PM_{2.5} concentration and vertical diffusion coefficient (K_z) averaged over the BTH region during the entire period and the first haze episode. Inside the parentheses are percentage changes relative to the NoAer case.

	$\Delta T2$ (°C)	$\Delta WS10$ (m s ⁻¹)	$\Delta RH2$ (%)	ΔPBL height (m)	$\Delta PM_{2.5}$ (µg m ⁻³)	ΔK_z (m ² s ⁻¹)
Study period (Feb 17 - Mar 12)						
All day	-1.4 (-69.4%)	-0.038 (-3.1%)	+8.7 (+14.9%)	-160.0 (-18.6%)	+20.0 (+28.6%)	-3.3 (-27.0%)
Daytime	-1.8 (-42.1%)	+0.028 (+1.9%)	+9.0 (+16.9%)	-267.1 (-22.4%)	+21.1 (+35.6%)	-6.7 (-27.6%)
First haze episode (Feb 20-26)						
All day	-1.8 (-59.7%)	-0.52 (-19.5%)	+9.8 (+12.4%)	-183.6 (-31.0%)	+45.1 (+38.7%)	-3.9 (-48.8%)
Daytime	-2.5 (-46.6%)	-0.59 (-19.8%)	+10.4 (+13.8%)	-307.3 (-37.6%)	+49.3 (+48.5%)	-8.3 (-51.9%)

Table 6. Same as Table 5 but for Beijing.

	$\Delta T2$ (°C)	$\Delta WS10$ (m s ⁻¹)	$\Delta RH2$ (%)	$\Delta PBLH$ (m)	$\Delta PM_{2.5}$ (µg m ⁻³)	ΔK_z (m ² s ⁻¹)
Study period (Feb 17 - Mar 12)						
All day	-1.6 (-39.1%)	-0.48 (-13.9%)	+11.8 (+23.3%)	-154.0 (-18.3%)	+30.1 (+29.8%)	-4.5 (-37.5%)
Daytime	-2.3 (-33.1%)	-0.52 (-13.9%)	+12.5 (+28.1%)	-282.7 (-22.5%)	+34.0 (+43.9%)	-9.6 (-38.8%)
First haze episode (Feb 20-26)						
All day	-2.1 (-46.1%)	-0.58 (-20.4%)	+17.0 (+24.5%)	-195.6 (-35.9%)	+68.0 (+39.1%)	-5.0 (-59.5%)
Daytime	-3.4 (-44.6%)	-0.78 (-23.9%)	+17.9 (+27.2%)	-358.3 (-45.5%)	+83.2 (+59.6%)	-11.0 (-63.2%)



Table 7. The model simulated feedback-induced changes (FULL minus NoAer) in BC, sulfate (SO_4^{2-}) and nitrate (NO_3^-) averaged over the BTH region and Beijing during the entire period and the first haze episode. Inside the parentheses are percentage changes relative to the NoAer case.

	Beijing-Tianjin-Hebei region (BTH)			Beijing		
	ΔBC ($\mu\text{g m}^{-3}$)	ΔSO_4^{2-} ($\mu\text{g m}^{-3}$)	ΔNO_3^- ($\mu\text{g m}^{-3}$)	ΔBC ($\mu\text{g m}^{-3}$)	ΔSO_4^{2-} ($\mu\text{g m}^{-3}$)	ΔNO_3^- ($\mu\text{g m}^{-3}$)
Study period (Feb 17 – Mar 12)						
All day	+0.9 (+25.1%)	+5.0 (+46.4%)	+6.8 (+37.3%)	+1.6 (+27.5%)	+8.4 (+58.5%)	+8.4 (+36.9%)
Daytime	+1.0 (+39.5%)	+5.4 (+60.2%)	+7.2 (+43.2%)	+1.9 (+51.5%)	+9.5 (+86.5%)	+9.5 (+48.8%)
First haze episode (Feb 20-26)						
All day	+1.9 (+32.9%)	+12.6 (+66.9%)	+14.6 (+40.9%)	+3.1 (+33.6%)	+22.3 (+81.8%)	+16.7 (+34.7%)
Daytime	+2.2 (+50.1%)	+13.8 (+81.4%)	+15.8 (+48.3%)	+4.1 (+62.3%)	+26.0 (+112.4%)	+20.9 (+51.5%)